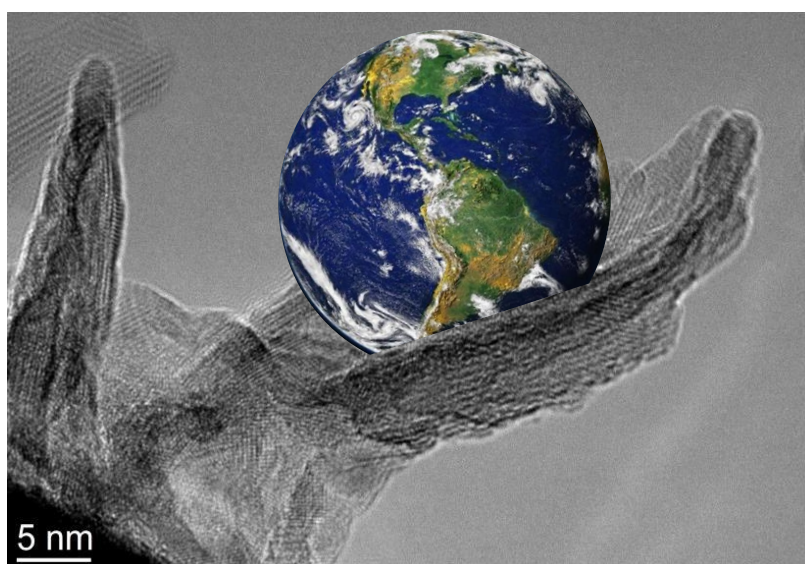# Water oxidation photocatalysis : Mn-based co-catalysts on TaON



**Marie-Mathilde Millet**

CGP student – Inorganic Chemistry student

**Internship Supervisor:**
Prof. Malte Behrens, Group Leader "Nanostructures" FHI
Cyriac Massué, PhD Student, FHI

**Pedagogical Supervisors:**
Dr. Bérangère Toury, Assistant professor at the University of Lyon
and Coordinator of the Master Inorganic Chemistry

Dr. Fabienne Fache, Research fellow CNRS and Chemistry coordinator CPE LYON

**MAX-PLANCK-GESELLSCHAFT**

Non confidential report

# Abstract

TaON was studied as a photocatalytic material for visible light driven water oxidation. Anomalies in the structure of the material such as lattice strain or oxygen deficiencies were shown to have a negative influence on its photocatalytic activity, as defects act as recombination centers for the photogenerated charge carriers. TaON was loaded with a manganese-based co-catalyst to enhance its activity. Mn deposition was realized following two procedures: deposition-precipitation and impregnation. The loading procedure was shown to have a great influence on the morphology and dispersion of the co-catalyst and therefore on its activity. Having showed more promising results, we deepened our investigations on the deposition-precipitation procedure and studied the influence of the pH-control agent on the morphology of the sample. To measure electrochemical and photocatalytical OER-activity we adapted to our system two testing methods based on the use of two sacrificial agents: the CAN test and the Ag test.

# Acknowledgment

First of all, I would like to express my sincere gratitude to Prof. Dr. Schlögl for giving me the opportunity of an internship at the FHI of the MPG.

I would like to thank Prof. Dr. Malte Behrens for welcoming me in his group, for his continuous advice, his trust, his encouragement and his patient supervision.

I am very grateful to Cyriac Massué, PhD student, for the continuous support and assistance in numerous ways during my internship and for his daily enthusiasm.

Furthermore, I would like to thank the rest of the "Nanostructures Group" for their help, their warm welcome and of course their good spirit.

In particular I would like to thank Jasmin Allan for the XRD and TGMS investigations, Wiebke Frandsen for the SEM and TEM pictures, Dr. Frank Girdies for the In-situ XRD investigations, Maike Hashagen for the BET measurements, Patrick Kast for the TPR trials and Achim Klein-Hoffmann for the XRF analysis. Some preliminary experimental work in this project was carried out by Dr. Nygil Thomas.

I address a special thank you to the partners of this project, and in particular Selivay Cosgun for the preparation of the TaON samples in the TU-Berlin.

Finally, I am sincerely grateful to my pedagogical supervisors, Dr. Fabienne Fache and Dr.Bérangère Toury for their time and patience, which were necessary for the coordination of a, simultaneous, engineering school Final Year Project and a University Master thesis, outside of France.
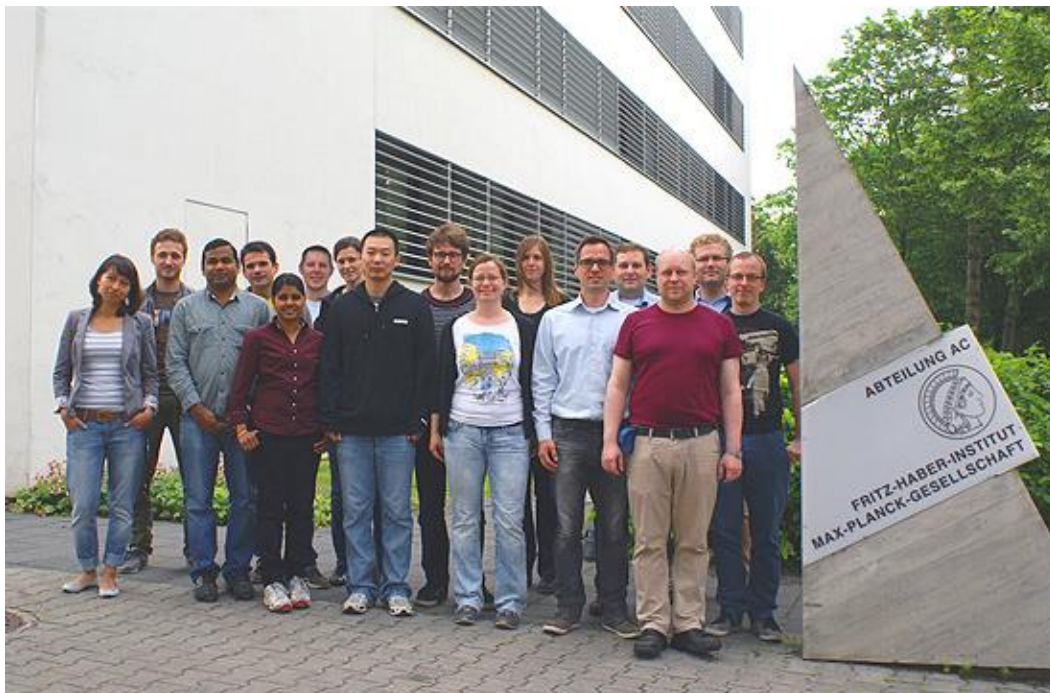


"The Nanostructure Group-FHI "

# Table of contents

# List of Figures and Tables

## Figures

## Tables

# List of Abbreviations

**HER**: Hydrogen Evolution Reaction

**OER**: Oxygen Evolution Reaction

**OEC**: Oxygen Evolution Complex

**WOC**: Water Oxidation Catalyst

**PSII**: Photosystem II

**CAN**: Cerium ammonium nitrate

# Introduction

## 1) Hydrogen fuels for renewable energy storage

In the past decades, clean and sustainable alternatives to fossil-fuel-based energy sources have been intensively researched in order to answer the increasing energy demand (predicted to increase by more than 40 percent by 2035)[a]. One approach for developing this kind of clean energy is in the use of hydrogen as an energy carrier. Hydrogen can be stored and transported, overcoming the transient nature of most renewable energy sources like wind or solar light irradiation. $H_2$ combustion in hydrogen fuel cells frees the stored energy, requires in addition to hydrogen only oxygen readily available from the atmosphere and produces only one harmless by-product: water[1].

Currently, the greater part of hydrogen production comes from the steam reforming of hydrocarbons[2], a process relying on fossil fuel sources and generating $CO_2$ as a by-product. A promising alternative is to obtain hydrogen from water splitting, following the equation:

$2H_2O \rightarrow 2H_2 + O_2$        $(E_0 = -1,23V)$
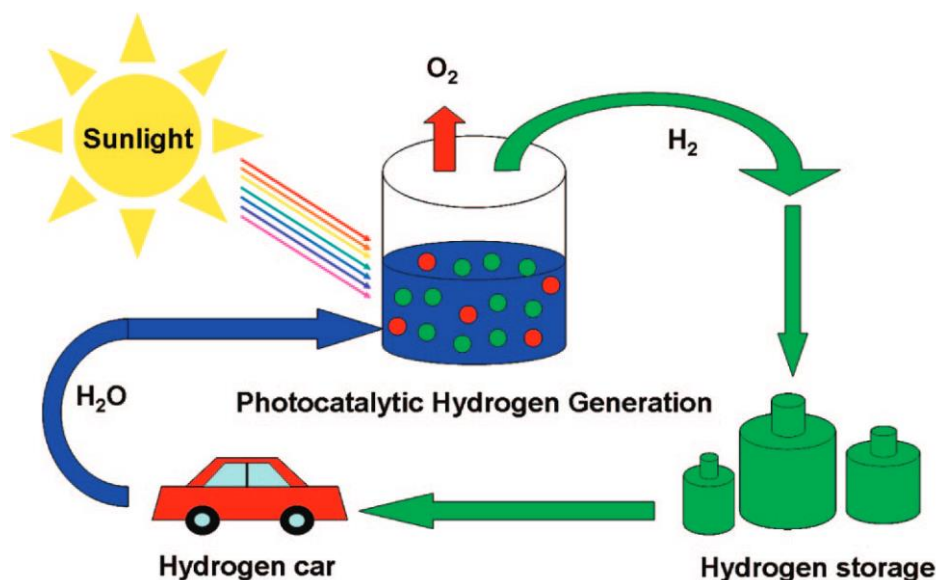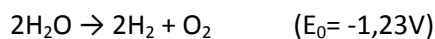


Figure 1 : Schematic representation of the Solar-hydrogen-cycle[3]

Water splitting consists of two half-reactions, which can be written in neutral/acidic conditions as[4]:

Oxgen Evolution Reaction (OER): $2H_2O \rightarrow O_2 + 4H^+ + 4e^-$
Hydrogen Evolution Reaction (HER): $4H^+ + 4e^- \rightarrow 2H_2$
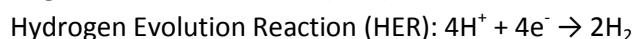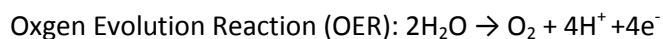
One way of inducing the splitting of water is through sunlight-driven photocatalysis. In this process the decomposition of water is, for example, driven by the light-induced creation of electron/hole pairs in a semiconductor. The light required for this process can be tapped from the greatest energy source available : the sun.

## 2) Semiconductors for photocatalytic water splitting

### a) Electronic band structure of semiconductors

Since the early work of Fujishima and Honda in the 1970s[5], semiconductors have been recognized as important candidates for photocatalytic water spitting because of their special electronic band structure (Figure 2).
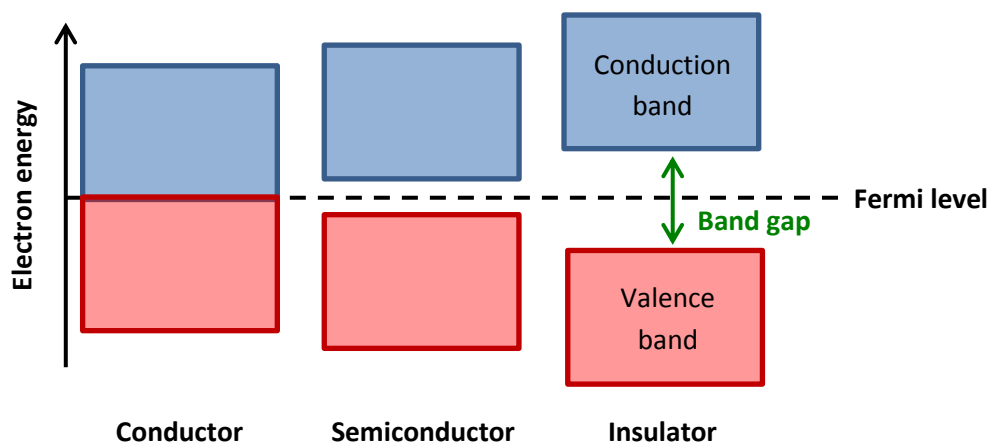


Figure 2 : Electronic band structure of conductor, semiconductor and insulator materials

A semiconductor's electronic structure possesses a valence band filled with electrons and separated from an unoccupied conduction band by an energy gap. If the material absorbs a photon of energy equal or greater to the band gap energy, an electron can be propelled into the conduction band. A positively charged hole is simultaneously created in the valence band. These electron/hole pairs can recombine or be involved in reactions with additional species (if the semiconductor meets the thermodynamic requirements of the reaction). If the electrochemical potential of the electron is reductive enough, it can reduce oxidized species in its vicinity; for instance a molecule absorbed on the surface of the semiconductor. In a similar fashion, holes can oxidize other species if their electrochemical potential is oxidative enough.

### b) Water splitting using semiconductors

In the case of water splitting, the splitting of two water molecules to produce an oxygen molecule and two hydrogen atoms consist of a 4-proton coupled electron transfer (PCET). After the creation of electron-hole pairs, those charge carriers migrate to the reacting species: water and protons. In order to provide enough electrochemical driving potential to the reacting species the electrons excited into the conduction band must be more reductive than the reduction potential of the protons, and the holes in the valence band must be more oxidative than the oxidation potential of water Cf Figure 3. Meaning that, the reduction potential of $H^+$ and the oxidation potential of $H_2O$ must be located between the edges of the valence band and the conduction band of the semiconductor. As a result of these requirements, the band-gap must be wider than 1,23 eV and its edges situated below and above the redox potentials of 0eV and 1,23eV.
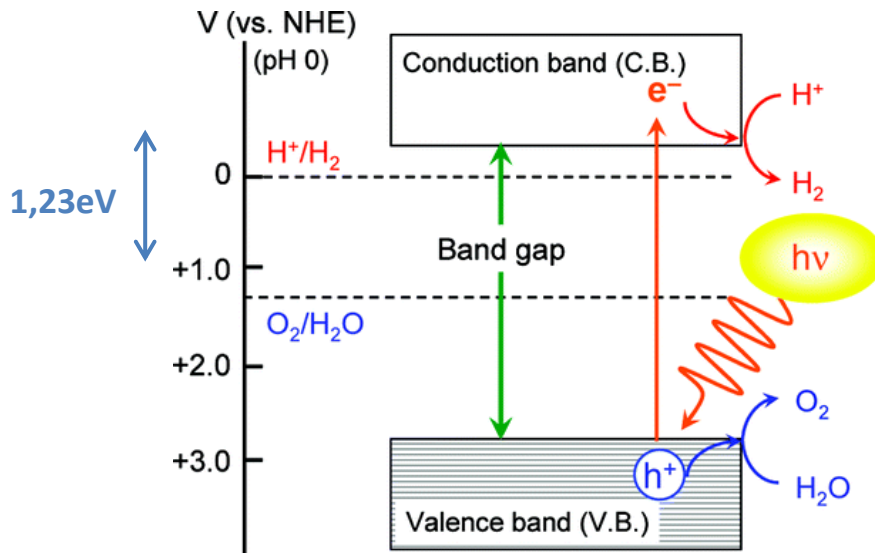
Figure 3 : Basic principle of overall water splitting on a heterogeneous photocatalyst[6]

The most critical part of this process is the OER: $2H_2O \rightarrow O_2 + 4H^+ + 4e^-$

Two water molecules must adsorb in close vicinity to one another in order to be able to combine to one dioxygen molecule downstream. Furthermore four holes with sufficient oxidizing power have to find these two water molecules in a short time frame. Otherwise, generated hydroxyl- and oxy-intermediates tend to undergo unwanted side-reactions (like the production of peroxy-species). This issue is closely linked to the adsorption behavior of the water species on the reaction sites and on the lifetime of charge-carriers. If electrons and holes recombine faster than they can reach one reaction site, the OER will not be complete and overall water splitting and hydrogen production will not take place.

The HER constitutes a much easier step of the water splitting reaction: HER : $4H^+ + 4e^- \rightarrow 2H_2$ [4].

The reaction only involves $2e^-$ and two protons to form a molecule of hydrogen and can follow two different reaction paths (enhancing the chances of reaction).Cf figure 4

$$H^+_{(aq)} + e^- \rightarrow H_{(ads)} \begin{cases} 2H_{(ads)} \rightarrow H_2 \\ H_{(ads)} + H^+_{(aq)} + e^- \rightarrow H_2 \end{cases}$$
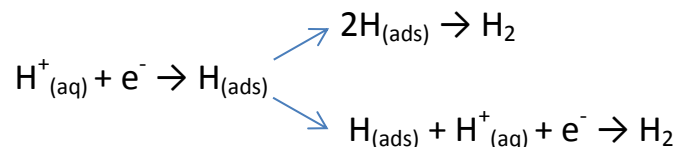
Figure 4: Decomposition of the hydrogen evolution reaction

### c) Considerations on the absorption region

In order to maximize the efficiency of the system, the semiconductor used as a photocatalyst should absorb as much sunlight as possible. $TiO_2$ for instance absorbs in the UV-range, where the intensity of the solar spectrum is far from its maximum. Indeed, the most intense area, in term of solar energy, is situated in the visible light region (390-700nm) cf. Figure 5. As a result, the photocatalyst's band gap will have to be smaller than 2,5eV (above this value we start to absorb UV radiations), but still bigger than 1,23eV.
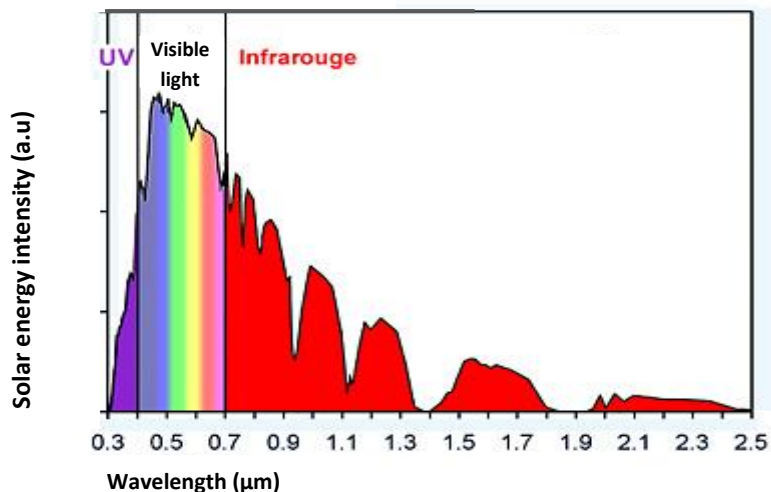
Figure 5: Solar radiation spectrum[b]

### d) Issues with recombination of charge carriers

Once created, the photoexcited species have to migrate to the surface of the semiconductor without recombination. This step, and its kinetic are strongly dependent on the structural and electronic properties of the photocatalyst. In general, high crystallinity has a positive influence on the activity, whereas structural defects act as recombination centres for photogenerated charge carriers [7].

### e) Improving the reactivity of the semiconductor: co-catalyst

Some semiconductors have an adequate electronic structure for visible light absorption and subsequent water splitting, however the reacting species may absorb little or weakly on their surface. In the case of OER, if the O-H bond is not weakened during absorption, additional overpotenials are required to drive the reaction, and recombination of charge carriers tend to dominate. In order to circumvent these issues, so-called co-catalysts are implemented into the system: these co-catalysts are loaded onto the surface of the photocatalyst to produce active sites and avoid recombination of the photogenerated charge carriers. They consist of metal or metal oxide particles that are usually good catalysts for the electrochemically driven OER and HER reactions. Reactive species should easily absorb on these co-catalysts, who should also attract charge carriers before they recombine and thus become reactions centres between charge carriers and active species.
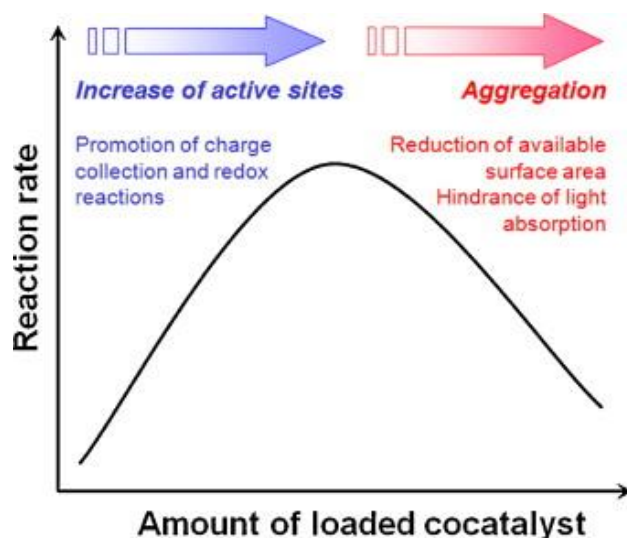


Figure 6 : Influence of cocatalyst loading on reactivity[8]

6

After selecting a HER- or OER-co-catalyst, several requirements need to be accounted for the synthesis. In classical heterogeneous catalysis for instance, well dispersed nanoparticles contribute to faster catalytic reactions, and an excessive loading tends to lower catalytic activity by decreasing the specific surface. In photocatalysis we observe the same "over-loading phenomenon", as an excessive loading of co-catalyst seems to obstruct light absorption. Cf volcano-type trend between loading amount and reactivity Figure 6.

## 1. *Hydrogen Evolution Reaction co-catalyst*

Even if the proton reduction reaction is less difficult to undergo than the water oxidation reaction, numerous investigations have been lead on HER co-catalyst deposition, mainly using, for this aim, Platinum nanoparticles. Indeed, Pt has been widely used as co-catalyst over many different kinds of semiconductors like metal-oxides[9], (oxy)sulphide[10], and oxinitrides[11]. Up until now, the highest activities for hydrogen production from photocatalytic water splitting using visible light were obtained with Pt loading as co-catalyst [12,13]. The processes of charge transfer between co-catalyst and host photocatalyst is illustrated Figure 7.
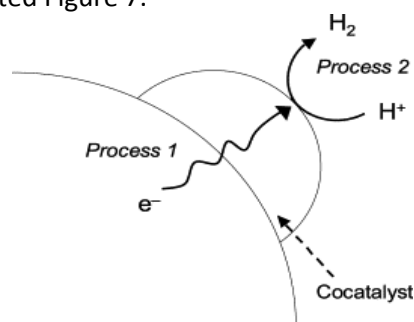


Figure 7 : Process of charge transfer between host photocatalyst and Hydrogen Evolution Catalyst[14]

When Pt is loaded onto the surface of the photocatalyst, the photogenerated electrons migrate to the surface of the host photocatalyst and are trapped by the noble metal. Noble metals play the role of "electron traps" because their Fermi energy level is lower than the one of semidconductor photocatalysts. The photogenerated holes stay in the host photocatalyst and migrate to its surface.[3]

Proton reduction is only possible if we have an efficient electron-holes separation (few recombinations), and efficient adsorption of the reactive specy ($H^+$), this is why the role played by the co-catalyst dispersed on the surface of the photocatalyst ist extremly important. It improves the overall photocatalytic activty as it favoures the adsorption of the protons and accelerates the reaction kinetics. The electrons find faster protons to reduce, improving charge separation, leading to a reduction of both bulk and surface recombinations[15].

## 2. *Oxygen Evolution Reaction co-catalyst*

The oxygen evolution reaction is much less understood due to the complexity of the reaction. However, some oxygen evolution cocatalyst deposition showed great success, using metal oxides such as $IrO_2$ or $Co_3O_4$[16,17]. Their loading at the surface of semiconductors resulted in an increase of the $O_2$ production[16,17]. Once again this enhancement of the activity is due to two complementary actions: the concentration of the holes and the amelioration of the water molecules adsorption. The holes find, more quickly, water molecules to oxidate and are, thereby, less likely to recombine [18]. Cf figure 8.
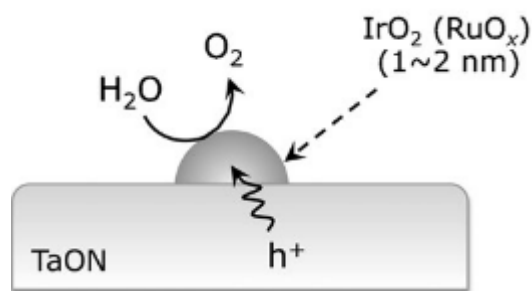
Figure 8 : Process of charge transfer between host photocatalyst and Oxygen Evolution Catalyst[19]

It was recently shown that the dispersion of oxygen evolution co-catalysts has a huge influence on the activity and the stability of the photocatalysts. It was shown that photogenerated holes have a very short diffusion length in the semiconductor materials, and therefore, highly dispersed co-catalyst particles are more efficient for charge carriers scavenging than the formation of aggregates[20], as it reduces the migration distance of the photogenerated holes.

## 3) Tantalum based photocatalysts

### a) TaON, a great semiconductor candidate

Among the potential candidates for water splitting, we find the tantalum-based semiconductors. One of the most important advantages of tantalum-based semiconductors is that their band gaps are suitable for visible-light driven overall water splitting. In particular, the valence band position can be tuned by the incorporation of nitride in tantalum oxides. In tantalum oxy-nitrides, the band energies are well positioned to undergo water splitting and with their narrow band gap they can absorb a large range of intense visible light (see Figure 9).
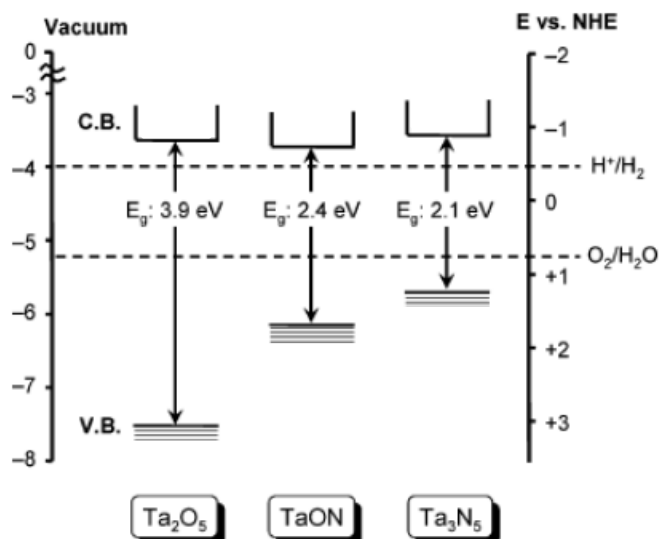


Figure 9 : Band structure of $Ta_2O_5$, TaON and $Ta_3N_5$ [6]

TaON is very stable inorganic compound that can be easily obtained from nitriding metal oxides under $NH_3$ flow, and have been demonstrated to absorb visible light. The group of Kazunari Domen has been intensively studying Ta-based photocatalysts and their application to overall water splitting. [21,22]

### b) Self-oxidative deactivation

In the case of TaON photocatalysts used for water splitting, the OER co-catalyst's properties as a hole scavenger are of heightened importance as it can help to avoid self-oxidative deactivation. The self-oxidative deactivation of the TaON is a phenomenon that was for the first time described by Domen's group in Japan[23]. The photogenerated holes, if not trapped by an efficient OER co-catalyst, can oxidize nitrogen anions $N^{3-}$ present in the lattice of the TaON semiconductor along the following reaction:

$$2N^{3-} + 6h^{+} \longrightarrow 2N_2$$
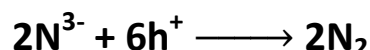
The formation of a photocatalytically inactive $Ta_2O_5$ phase leads to a decrease of the efficiency and the stability of the material.

## 4) Mn-oxides as water oxidation catalyst

In nature, water oxidation is catalysed within photosystem II (PSII). The active site for water-oxidation: the oxygen evolution complex (OEC)[24,25] is made of abundant elements, and therefore many research groups are following a biomimetic approach[25,26] in order to develop affordable synthetic catalyst for the OER. Understanding the complex PSII has taken slow but continuous steps, with a crystal structure of PSII finally published in 2011 by Umena and co-workers, showing the structure of the OEC to be a $CaMn_4O_5$ complex[27].

Another approach has been a careful screening of available earth abundant candidates using DFT methods.[15,28]

Both approaches, leads us to the use of manganese, as it is an abundant, non-toxic element, that might be a very promising candidates to realize the artificial photosynthesis.[29]

Manganese oxides, and especially $MnO_2$ compounds have showed excellent turnover frequencies for electrochemical water oxidation[30] and have been described in a large number of publications, as efficient oxygen evolution catalysts [31-35].

The price, the abundance and the catalytic activity of manganese oxides, make them very interesting candidates for water splitting co-catalyst.

## 5) Testing the photocatalysts

### a) Artificial photosynthetic cell

The ultimate goal of the development of efficient photocatalysts, is the fabrication of an "artificial photosynthetic device". A concrete example of such device is Nocera's famous artificial leaf[25] cf figure 10. Unfortunately, the design of electrode and the testing, is an energy and time-consuming process, inadequate for catalysts screening. Therefore, we decided to resort to the use of sacrificial agents.
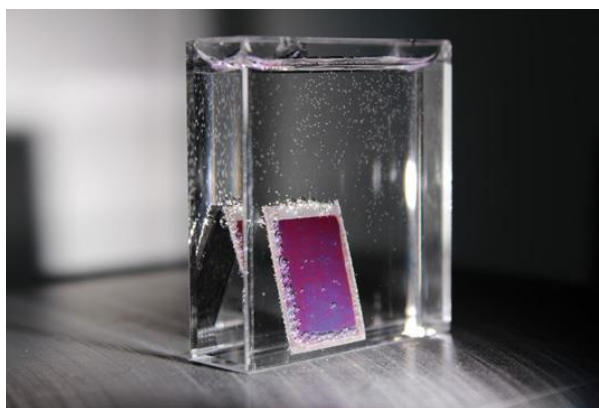
Figure 10: Nocera's artificial leaf [c]

### b) Sacrificial agents

Electrochemical methods can be used to evaluate the behaviour of water oxidation catalysts (WOCs) under conditions similar to those inside a functional artificial photosynthetic cell, but even those methods require specialized equipment and considerable expertise[36,37]. In catalyst screening and optimization, efficiency is frequently measured with the help of a sacrificial agent; according to the reaction path presented Figure 11. [38]

$$4Ox^{n+} + 2H_2O \xrightarrow{catalyst} 4Ox^{(n-1)+} + O_2 + 4H^+$$
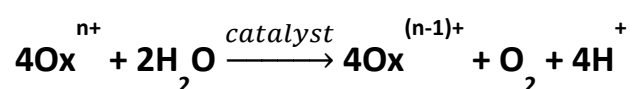
Figure 11 : Reaction equation of sacrificial oxidants

Another huge advantage of the use of sacrificial agents, apart from their simplicity of use, is that they make possible studies in bulk solution. Studies in bulk solutions give bigger $O_2$ answers, and facilitate analysis. Sacrificial agents however only mimic what happens in a photosynthetic cell, Information obtained by such means is therefore mostly used for screening and serves as qualitative but not quantitative information on the activity of the photocatalytic system.

### 1. Testing of the electrochemical activity of the co-catatlyst : the CAN-test

For testing the activity of redox-catalysts, also used as co-catalysts in photochemical systems, there are many different sacrificial oxidants available, such as $(NH_4)_2Ce(NO_3)_6$ and $[Ru(bpy)_3]$. Cerium Ammonium nitrate (CAN) has been described as good mimic of the OER reaction, with suitable redox potential[38]. However it is only stable at very low pHs. Hence corrosion phenomena, especially for Mn oxides play a major role.

CAN is a powerful one electron oxidant that has been widely used to characterize WOCs. It oxidizes water along the following equation:

$$4Ce^{4+} + 2H_2O \xrightarrow{catalyst} 4Ce^{3+} + O_2 + 4H^+$$
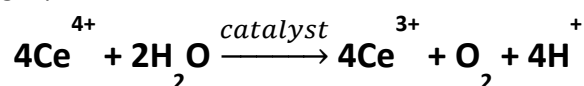
The rate of the reaction depends on the activity of the redox-catalyst. CAN is readily available commercially and remains stable in aqueous solution for a reasonable amount of time. One of the main disadvantages of the CAN is that it is only stable at low pH; a CAN solution generally has a pH of 0,9[39]. Furthermore, CAN is a photoactive compound itself. This restrains the applicability of CAN for studying WOCs under "artificial photosynthetic cell" conditions. However, the CAN test is very suitable to screen the redox-catalytic properties of the co-catalyst in the dark in a purely

electrochemical, i.e. non-photocatalytic, experiment without participation of the photocatalyst. This activity is a pre-requisite for high performance of the co-catalyst/photocatalyst composite and the test thus gives valuable information on the co-catalyst.

## 2. Testing of the photochemical activity of the co-catalysts: the Ag-test

In order to assess the photochemical activity of the system, silver nitrate can be used as a sacrificial agent. Its main advantage over the ceric ammonium nitrate is that, it is not a photoactive material and works at mildly basic pHs.

Silver nitrate is a one-electron oxidant, which has been widely used to realize photocatalytic testing of semiconductor such as TaON[40,41]. It reacts along the following equation[23]:

$$4\ Ag^+ + 2\ H_2O \xrightarrow{\text{catalyst}} 4Ag + O_2 + 4H^+$$
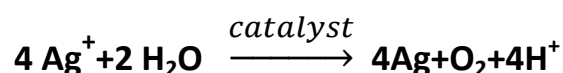
With increasing pH, the redox potential of water decreases, which facilitates water oxidation for holes with a stable redox potential. At the same time, the redox potential of silver allows it to accept an electron from the conduction band of the semiconductor, accelerating the kinetics of the reaction, and avoiding charge carriers recombination. As we can see on the Pourbaix diagram of silver presented figure 12, in basic conditions, $Ag^+$ tend to precipitate to form $Ag_2O_{(s)}$ insoluble in water. Consequently, we will have to work at the highest pH possible, but still smaller than the precipitation pH of $Ag_2O_{(s)}$.

*Example: for a 0,01M solution we will try to work at pH 8 to optimize the oxygen answer.*
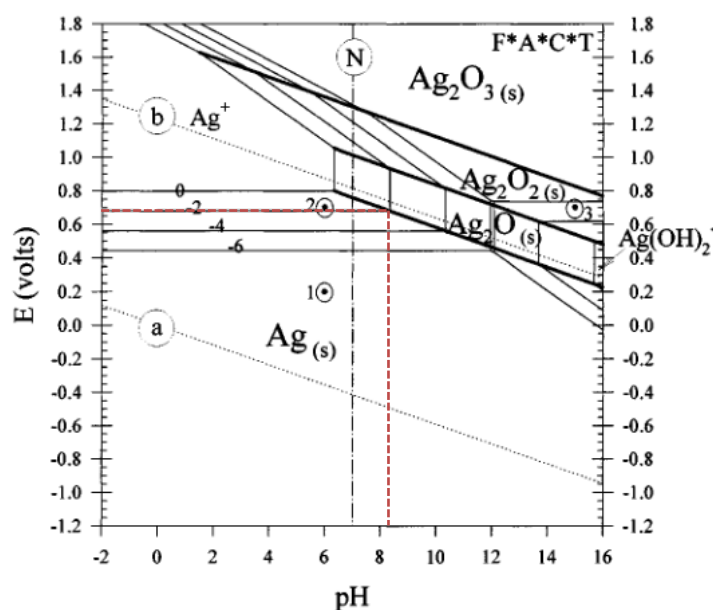


Figure 12: The Ag Pourbaix diagram at 298K. Concentration of aqueous species range from 1 to $10^{-6}$. "a" corresponds the reduction potential of protons and "b" to the oxidation potential of water[d]

$La_2O_3$ is typically used as a buffer, to maintain the pH of the solution at the desired value.[40]

The inconvenient of the silver test, is that we observe a fast decrease of the oxygen evolution, due to, on the one side to the decrease of $Ag^+$ concentration, and on the other side, due to the coverage of the TaON surface with metallic Ag particles that obstructs photon absorption by the TaON[42].

# 6) Conclusion and objectives

Being able to produce hydrogen out of water and sunlight is an economic and ecological challenge. In order to achieve this, the kinetics of the OER has to be improved. Researchers have been studying numerous semiconductor materials. Among the potential candidates, we find the tantalum oxy-nitride, an easily synthesized material that possesses all the criteria to undergo visible light driven water splitting. Our study will be focused on the improvement of the photocatalytic activity of TaON as an "artificial photosynthesis" anodic material. The group of Kazunari Domen significantly improved the activity of the TaON using expensive and rare co-catalysts. For this project we decided to test the suitability of earth-abundant manganese as OER-co-catalyst as it has long been known for its properties as a good OER catalyst.

This project was realized in frame of the "Priority Program (PP) 1613 – SolarH2 – Project" of the Deutsche Forschungsgemeinschaft (DFG), in the sub-group "Nanostructured Ta-oxide nitride and Chalcopyrite-based Thin Film Composites and Co-Catalysts for Visible Light-driven Overall Water Splitting". This project is realized in collaboration with Dr. Malte Behrens, Fritz-Haber-Institut der Max-Planck-Gesellschaft, Professor Dr. Martin Lerch, Dr. Anna Fischer from the Technical University of Berlin, and the Professor Dr. Thomas Schedel-Niedrig from the Helmholtz-Zentrum of Berlin. The project at the Fritz-Haber-Institut and this Thesis focuse on the loading and characterization of Mn-based co-catalyst on TaON photocatalysts.

The loading of the Mn-co-catalyst on the TaON support was realized following two synthesis strategies: constant-pH symproportionation of $Mn^{2+}$ and $MnO4^{-}$ in the presence of TaON and impregnation of the TaON with $Mn^{2+}$. It was followed by calcination to obtain manganese between the oxidation state +3 and +4, active for the OER[29]. The products were analysed using XRD, TGMS, SEM, and TEM. The redox-catalytical activity of the Mn-co-catalysts was assessed with the CAN-test and the photochemical activity of the $MnO_x$/TaON composite was assessed using the Ag-test.

# Experimental

## 1) Doped TaON synthesis

### a) TaON

The TaON was synthesized by the Technical University of Berlin, a partner of this project. Crystalline $Ta_2O_5$ was heated at 1050°C during 12h and flushed with 10L/h of $NH_3$ and 0,3L/h of $O_2$.[43]

### b) Zeta potential

Before the loading of manganese oxides on the TaON surface, we need to make sure that the manganese ions are going to be absorbed at its surface. For this aim we defined the isoelectric point of a TaON suspension (zeta potential=0). The zeta potential of a sonicated solution (1h) of 10mg of TaON in 100ml of water was measured over a large range of pH. To vary the pH of the solution, $HNO_3$ (1M) and KOH (1M) were used. Zeta-potentials were measured by a "Malvern instruments Zetasizer Nano-ZS- 633nm Laser" equipped with a"Laser Doppler Velocimetry"
A description of the measurement method is presented APPENDIX 1.

### c) Deposition-precipitation

### 1. Principle

One of the loading method we used was through deposition-precipitation. We first deposited $Mn^{2+}$ ions at the surface of the TaON, and then progressively added $MnO^{4-}$ ions to undergo the following symproportionation reaction: $3Mn^{2+} + 2MnO_4^- + H_2O \rightarrow 5MnO_2 + 4H^+$
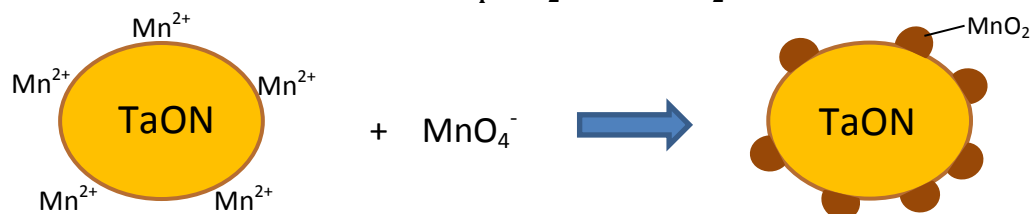


Figure 13 : schematic representation of the deposition-precipitation reaction
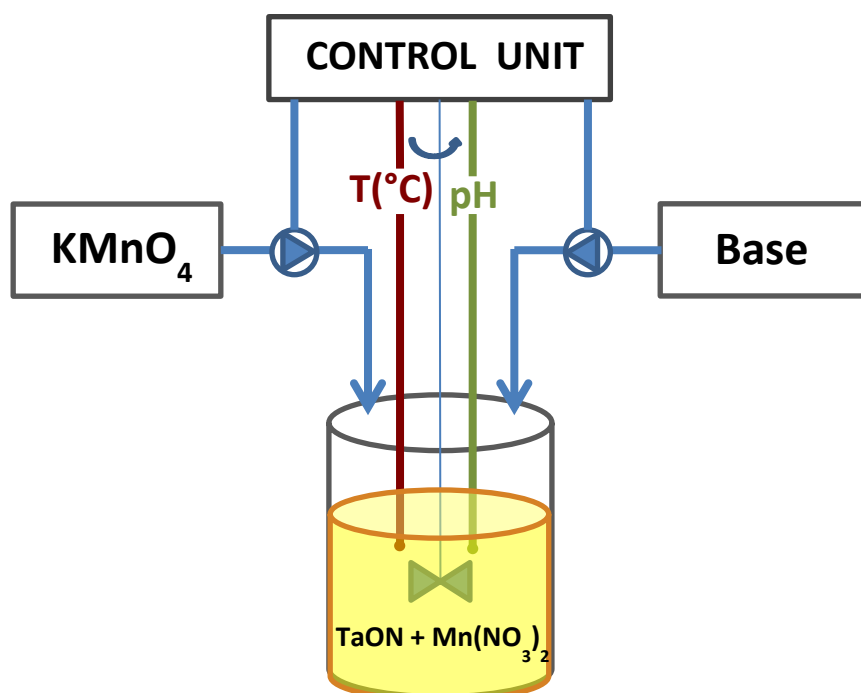


Figure 14 : Schematic representation of the LabMax reactor

In order for the $Mn^{2+}$ ions to be fixed at the surface of the TaON, we need to work at a pH far from the isoelectric point of the TaON solution. At the isoelectric point (zeta potential=0), the surface of the TaON will not be charged and the manganese ions won't be adsorbed at its surface. We will always work at a higher pH than the one of the isoelectric point, to obtain negatively charged TaON particles. The pH-controlled symproportionation of $KMnO_4$ and $Mn^{2+}$ adsorbed on TaON is conducted in an automated laboratory reactor system (Mettler-Toledo LabMax). This LabMax reactor allows us to control synthesis parameters such as: addition rate of the reactives, agitation, temperature and pH. Cf figure 14.

A main advantage of the LabMax reactor is the possibility to control the pH during the reaction. Working at constant pH allows every precipitation reaction to occur under the exact same conditions and for the $Mn^{2+}$ ions to remain attached to the surface of the TaON, and thereby increase the reproducibility of the synthesis. As seen above, the symproportionation of manganese releases protons; in order to work at a constant pH, an alkaline solution is added when needed to maintain the pH at the desired value, while the reactant (in our case $KMnO_4$) is added at a constant rate. After the symproportionation reaction, an ageing treatment (1h,50°C) is necessary to complete the nitrate ions removal.

The addition of $KMnO_4$, of the alkaline solution, the pH and the temperature are monitored during the synthesis. An example is presented in Figure 15.
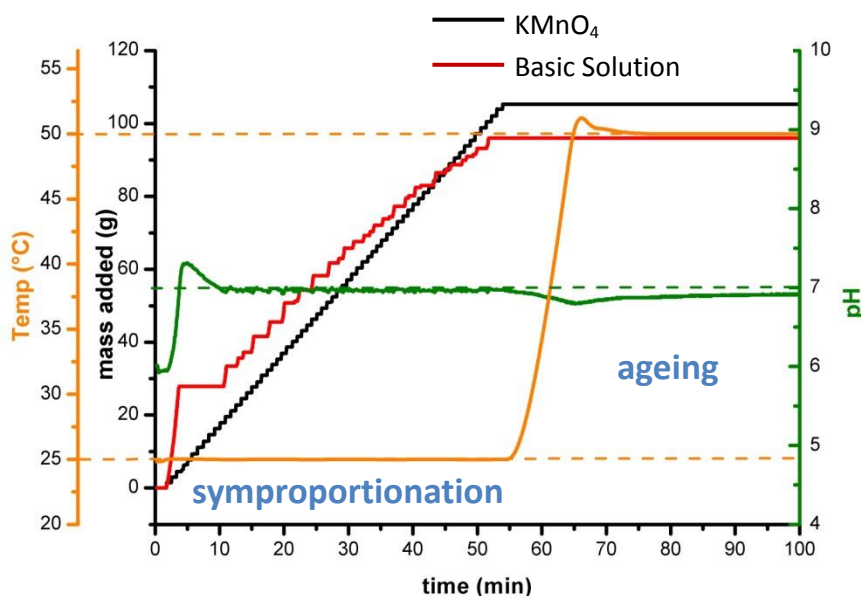


Figure 15 : Monitoring of a LabMax synthesis at pH=7

## 2. Preparation of symproportionated samples

Example for the 0,8% weight ratio Mn/TaON sample:

2g of TaON were added to 300mL of deionized water and sonicated for 1hour. After sonication, 45,72mg of $Mn(NO_3)_2.4H_2O$ were added to the solution and poured inside the LabMax reactor. The solution needed for the symproportionation was prepared by adding 107,9mg of $KMnO_4$ to 1L of deionized water. The basic solution used to neutralize the formed protons was prepared by adding

120mg of NaOH in 1L of deionized water. The LabMax program was set to add progressively 105g of the KMnO4 solution (0,1mol of $KMnO_4$) and the pH was set at 7.

The suspension obtained was filtered and washed until the conductivity of the washing waters was under a reference value of 0,05mS. It was then dried in air for 10hours at 60°C, and calcinated in air for 10hours at 300°C. (Oven heating rate: 5°C/min)

### d) Impregnation

### 1. Principle

A second batch of Mn-loaded TaON samples was prepared by impregnation of TaON with $Mn(NO_3)_2$. In this method, the TaON powder is mixed with a small volume of manganese nitrate solution, through the drying of the sample, the manganese nitrate is going to form a more or less homogenous envelope, which will, during the calcination in air, aggregate and be oxidized into manganese oxides.
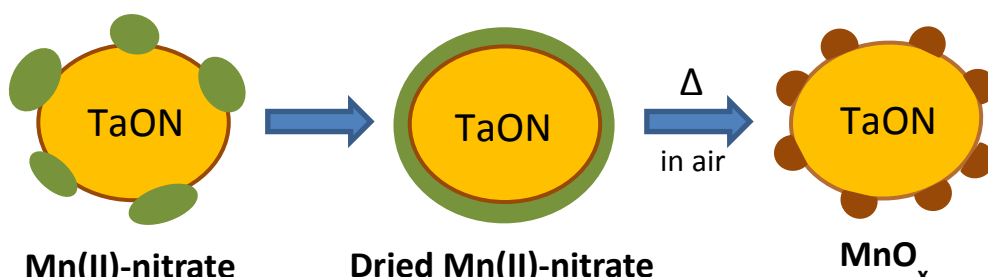


Figure 16: Schematic representation of the impregnation

### 2. Preparation of the impregnated oxides

Example for the 0,4% weight ratio  Mn/TaON sample:

A solution of manganese nitrates was prepared by adding 325,9mg of $Mn(NO_3)_2.4H_2O$ in200mL of deionized water. 2mL of this solution were added in a very small crucible. A solution of diluted ammonia was prepared (6,25mg/L) and two drops of it were added to the manganese solution inside the crucible. 178,3mg of TaON were then added to the mixture and it was let to stir for 48h. After 48h, all the water evaporated and the crude product was calcined at 300°C for 8h.

## 2) Electrochemical test
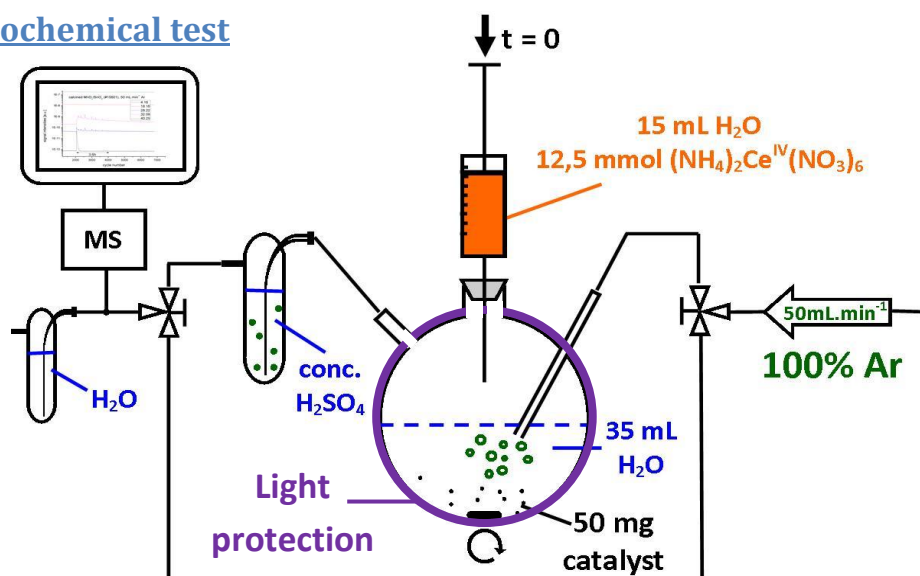


Figure 17 : Schematic representation of the electrocatalytic testing reactor

### a) Principle

The testing reactor consists of a 100mL three neck round bottom flask, flushed with argon with a rate of 50mL/min. The gas lines are made of air-tight stainless steel lines and Swagelok valves. The out coming gas is bubbled through a concentrated sulphuric acid solution for drying, and analysed using a mass spectrometer (Pfeiffer QMS200 OmniStar quadrupole mass spectrometer). The flask is shielded from the sun with an aluminium foil. Cf. figure 17.

### b) Sample preparation and testing

50mg of catalyst are added to 35mL of deionized water in a 100mL three neck round bottom flask and left to sonicate for 10 minutes. The solution is than flushed with argon for 25 min. The mass spectrometer signal is calibrated with 3 injections of known volumes of pure oxygen. 6,85g of $(NH_4)_2Ce(NO_3)_6$ are added to 15mL of deionized water, stirred and flushed with argon for 25minutes. The solution is then injected into the flask through the air-tight septum.

## 3) Photocatalytic test

### a) Principle
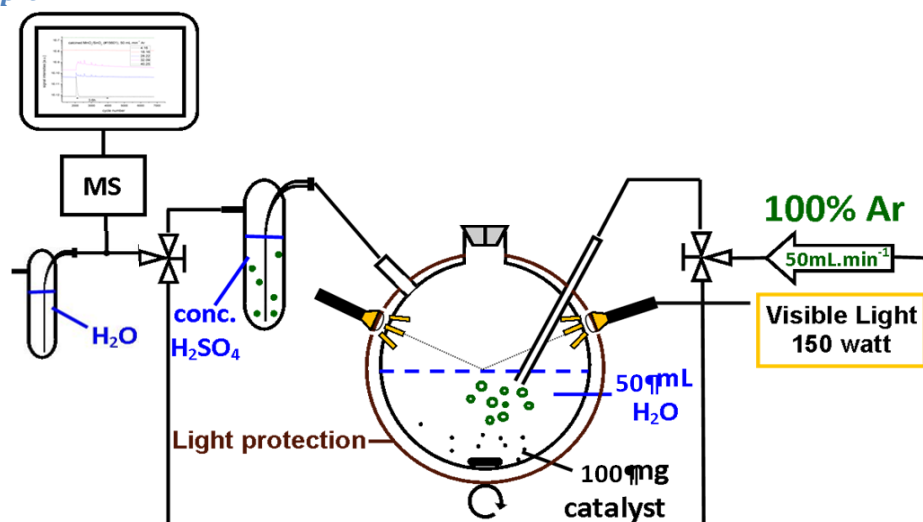


Figure 18: schematic representation of the photocatalytic testing reactor

The testing reactor consists of a 100mL three neck round bottom flask, flushed with argon with a rate of 50mL/min The gas lines are made of air-tight stainless steel lines and Swagelok valves. The out coming gas is bubbled through a concentrated sulphuric acid solution for drying, and analysed using a mass spectrometer (Pfeiffer QMS200 OmniStar quadrupole mass spectrometer). The flask is covered with aluminium and two orifices are made in the foil at fixed positions to illuminate the reaction with visible light. The visible light comes from a 150Watt halogen lamp (SCHOTT KL 1500 electronics), and was fitted with a visible light filter (>400nm) .Cf. figure 18.

### b) Preparation of the sample and test

100mg of catalyst are added to 50mL of deionized water in a 100mL three neck round bottom flask protected from light with an aluminium foil. 0,05g of $La_2O_3$ , and 0,085g of $AgNO_3$ are added to the solution. The solution is left to sonicate for 10min. The solution is than flushed with argon for 25minutes. The mass spectrometer signal is calibrated with 3 injections of known volumes of pure oxygen, and when the signal comes back to its initial level, two holes are made inside the aluminium foil at fixed positions and the solution is irradiated (through these holes) for 2hours.

# 4) Analysis methods

### a) XRD

X-ray diffraction patterns were measured using a transmission diffractometer (STOE STADI P) equipped with a primary focusing Ge monochromator (Cu Kα1 radiation). Theoretical background of the method is presented APPENDIX 2.

### b) TGMS

Thermal analyses were performed on a Netzsch Jupiter STA 449C thermobalance equipped with a Pfeiffer QMS200-OmniStar-quadrupole mass spectrometer for analyzing the exhausted gases. (Parameters:21%$O_2$/Ar, 5°C/min). Theoretical background of the method is presented APPENDIX 3.

### c) SEM-EDX

The morphology and local content of manganese was studied by scanning electron microscopy (SEM) coupled with energy-dispersive X-ray analysis (EDX) using a Hitachi S-4800 electron microscope operating at 2kV in secondary electron (SE) mode. Theoretical background of the method is presented APPENDIX 4.

### d) TEM

A FEI Titan 80-300 microscope operated at 300 kV and equipped with a field emission gun, CEOS Cs-Corrector, the Gatan imaging filter, and energy dispersive X-ray (EDX) analyzer was used for TEM investigations. Theoretical background of the method is presented APPENDIX 5.

### e) TRPL

Time-Resolved Photoluminescence (TRPL) measurements were lead by A.Bartelt and S. Müller at the *Helmholtz Zentrum Berlin*. No precisions were communicated yet on the testing device. Theoretical background of the method is presented APPENDIX 6.

### f) XRF

For elementary analysis, the samples and corresponding standards were mixed with lithiumtetraborate flux (FX-X100, Fluxana) and fused in a Vulcan Fusion Machine at 900°C (HD Electronic & Elektrotechnik GmBH) under formation of flat molten glass discs, which were analyzed by X-Ray Fluorescence spectroscopy using the spectrometer Pioneer S4 (Bruker AXS GmbH)
Theoretical background of the method is presented APPENDIX 7.

# Results and discussion

## 1) TaON

The TaON was synthesized by a partner Laboratory at the Technical University of Berlin. After receiving the samples, they were analysed by XRD, TGMS, and tested in our electrocatalytic testing reactor. Some of the samples received, showed differences in terms of: colours, crystallinity and photoluminescent lifetime.

### a) Strained vs. Unstrained TaON

#### 1. XRD measurements

The first difference that we observed, was in-between the different XRD patterns of the TaON samples. Indeed, some samples showed an anisotropic peak broadening as shown figure 19 and 20.
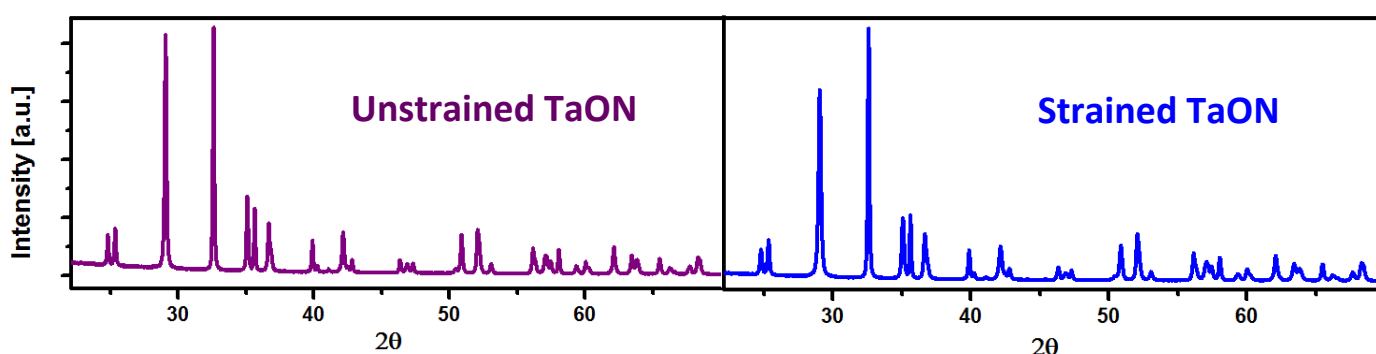


Figure 19: XRD diffractogram of an unstrained and a strained TaON sample
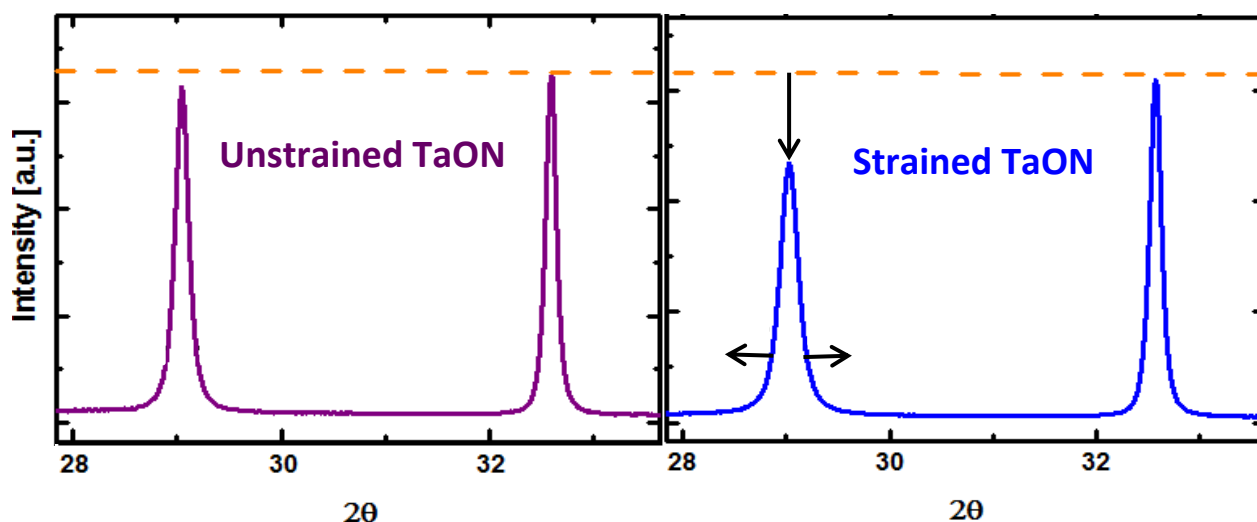


Figure 20: XRD diffractogram of an unstrained and a strained TaON sample, zoom on the 2θ=[28-34] region

This peak broadening can be explained by two different phenomena, a size effect and a strain effect. The general concept of strain describes a tensorial quantity, and is directly related to the elasticity of a material. A body under elastic deformation experiences internal resistance. The amount of deformation caused is called strain and the corresponding force, the stress. As in this case no external force was applied on the solid we might attribute this phenomenon to a lattice mismatched

film growth that occurred during the synthesis[44]. The intensity of the strain of these samples is listed Table 1. The method used to determine the strain factors is described APPENDIX 8.

| Sample | "strain factor" |
|---|---|
| "unstrained" TaON | 0,00 |
| "strained" TaON | 0,12 |

Table 1: Strain factor of the different TaON

The second phenomenon responsible for these differences in the XRD patterns is the size effect, as the presence of smaller coherent domains leads to a peak broadening and anisotopic domain morphologies can lead to anisotropic peak broadening.

## 2. TEM analysis

In order to have a better understanding of this phenomenon, TEM analyses were performed on strained and unstrained TaON in order to relate the average structural information from XRD with direct local structural observations of individual crystallites.
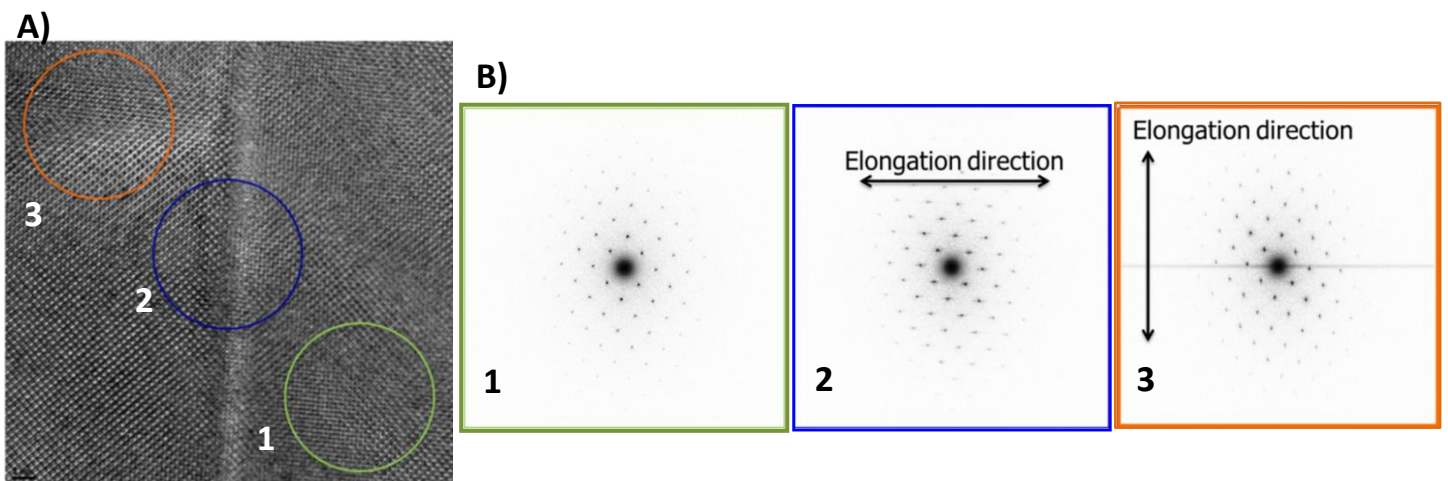


Figure 21: A)TEM picture of a strained TaON sample B)Fast Fourier's transformation of the circled regions

Using TEM methods, the study of the TaON samples that didn't show strain in XRD, revealed a high local regularity of the lattice, confirmed by FFT (Fast Fourier Transform). While spot n°1 in Fig. 21 exhibits a regular FFT spectrum, the second and the third spots show elongations along directions that result from straining of the crystal lattice along these same directions (100 and 010). Further analysis, presented figure 22.A) shows that the straining evidenced in the FFT spectra results from disruptions in the crystal lattice. In Figure 22.A), white lines correspond to disruptions in the continuity of the N- and O- arrangements (stacking faults). The IFFT analysis of the same picture highlights the disruptions of the lattice that ultimately produce the strain.

This phenomenon is not to be observed on unstrained TaON, and is considered responsible for the straining which leads to anisotropic peak broadening. On the one side this slipping induces tensions inside the structure causing the strain. On the other side these slipping planes reduces the size of coherent crystalline domains, which is, just like the strain, responsible for the peak broadening observed figure 20.
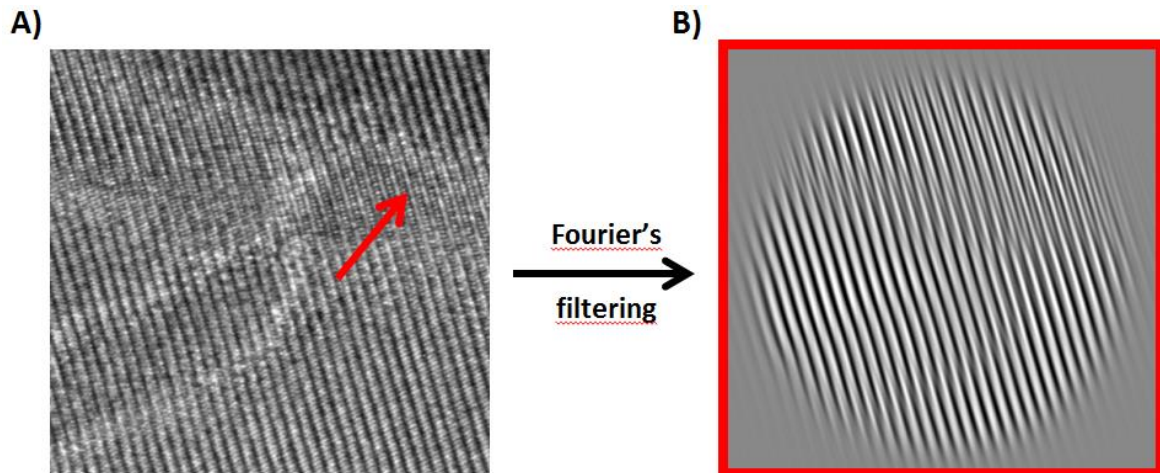


Figure 22: A) TEM picture of the strained material B) enlargment of the pointed area after IFFT

### b) *Photoluminescence*
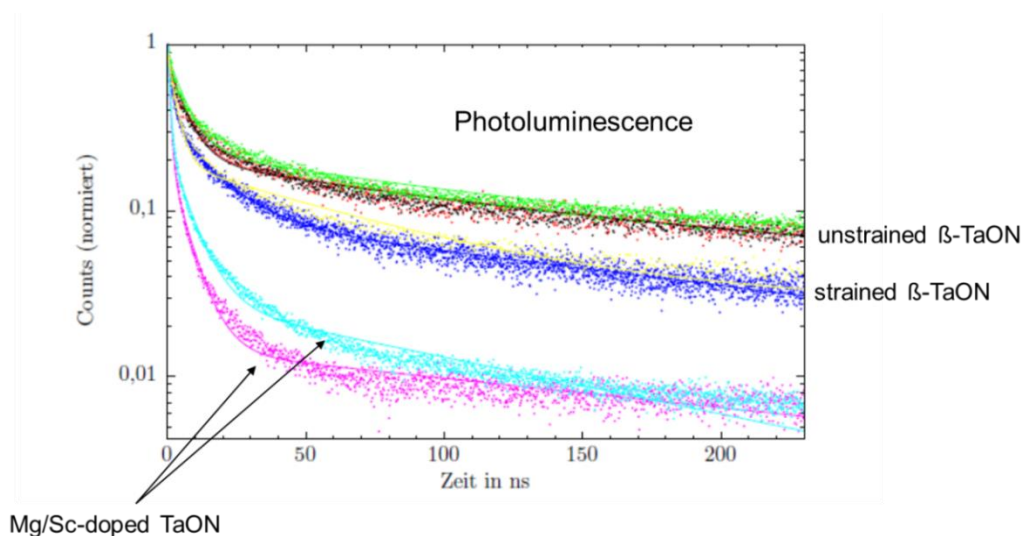


Figure 23: Time-Resolved Photoluminescence experiment on different TaON

As seen earlier the efficiency of a semiconductor depends a lot on its tendency to recombine the photogenerated species. The longer holes and electrons take to recombine, the longer they remain available for reaction. Thanks to Time-Resolved Photoluminescence experiments presented Figure 22, we see that the charge carriers of unstrained TaON have a longer life-time than strained TaON. Based on these results, it was decided to avoid the use of strained TaON.

*c) Yellow vs. Green TaON*

*1. XRD analysis*
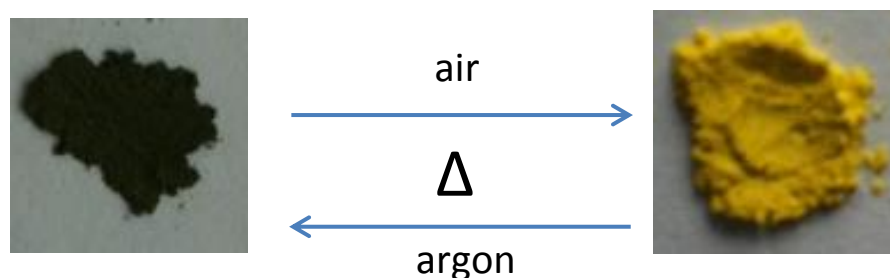


Figure 24:  Pictures and transition path of green to yellow and vice -versa

Unstrained TaON was received in two colors: yellow and green. In order to study the transition of green to yellow TaON and vice-versa, we investigated the behavior of the samples under various gas atmospheres. We noticed that calcination of the yellow TaON at 800°C for two hours in Argon leads to green TaON, while the calcination of green samples at 400°C for 6hours in air reversibly yields the yellow sample.

These results lead us to think that the green color is linked to the creation of oxygen vacancies. UV-Vis investigation will be necessary to validate this hypothesis.

*2. Photocatalytic activity*

To compare the photocatalytic activity of the two samples, we used the silver test. The results of the experiments are presented figure 25.

After one hour of reaction, the oxygen production induced by the yellow TaON is more than two times bigger than the one of the green sample.
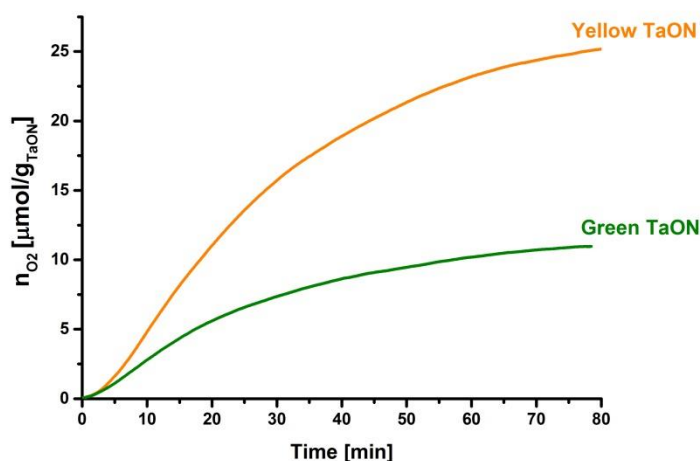


Figure 25: photocatalytic oxygen production over time [Silver Test]

This can be explained by a change in the light absorption behavior (the dark green sample could obstruct light in the reactor). Another likely explanation could be based on the increased occurrence of O-deficiencies in the green sample. These O-deficiencies, could act as recombination centers or

traps for the charge carriers and reduce the photocatalytic activity of the sample by reducing the concentration of charge carriers.

### d) Iso electric point of the TaON
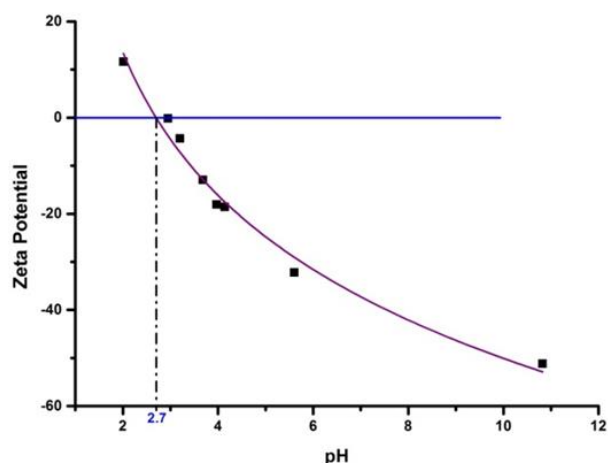


Figure 26: Evolution of the zeta potential with the pH

As seen earlier, the determination of the isoelectric point of the TaON is an essential step of the synthesis to assure an efficient fixation of the manganese species at its surface. In the literature[45], we found the isoelectric point for β-TaON at pH=2,5, and the one that we measured for the β-TaON received from our partners is, as represented Figure 26, at pH=2,7. This value remained unchanged for the unstrained, strained and green TaON. For all the synthesis (deposition-precipitation and impregnation) we made sure that we are working above this pH value, to assure the efficient anchoring of the manganese at the surface of the semi-conductor.

## 2) Analysis of the loaded samples

In order to further improve the photocatalytic activity of the reference TaON-sample (unstrained, yellow) the TaON was loaded with various amounts of Mn following the two synthesis procedures described in the *EXPEXIMENTAL, part 1)c) and d).*

We needed to determine the right thermal treatment conditions in order to activate the co-catalyst without destroying the TaON semi-conductor. The synthesis parameters should be tuned to yield a Mn-particle dispersion that allows maximal light absorption by the TaON while guaranteeing good electrical contact of the co-catalyst/support-interface.

### a) TGMS

Thermogravimetric measurements coupled with mass spectrometry analysis were led on three samples: pure TaON, TaON-5%Mn obtained through impregnation and TaON-0,8%Mn obtained through symproportionation cf Figure 27.

The sample mass of pure unloaded, unstrained TaON (green curve on in Fig.27) remains stable until approximately 750°C. At higher temperatures a marked increase of sample mass coincides with a sharp $N_2$ peak at 794°C. XRD analysis of the sample after TGMS measurement shows that after calcination at 1000°C the only product left is $Ta_2O_5$. At temperatures higher than 750°C, pure TaON hence decomposes to $Ta_2O_5$, a photocatalytically inactive material.

For the loaded samples it seems that the higher the loading, the earlier the material starts its decomposition. For both the impregnated and symproportionated samples, the sample mass gain shows an onset at 500°C and a concomitant rise in the $N_2$-signal. Thus it can be inferred that manganese present on the surface of the TaON destabilizes the TaON structure if the calcination temperature is chosen too high. For both loaded samples two nitrogen peaks are observed: a sharp and intense peak similar to the $N_2$-peak of the pure TaON but at lower temperatures and a second broad peak closer to the onset of mass gain. This peak might correspond to species in close contact with the manganese particles, which decompose earlier. A likely explanation would be that MnOx particles on the surface act as catalysts for activated oxygen species at high temperatures. The activated oxygen species react with surface TaON, forming surface Ta-oxides and are responsible for the early onset of TaON-decomposition.

Finally the impregnated sample shows a NO peak around 200°C corresponding to the elimination of the residual nitrates still present from the synthesis.

This experiment shows that the calcination temperature of the Mn-loaded TaON-samples have to be conducted at temperatures below 500°C in order to avoid early decomposition of the semi-conductor and above 250°C in order to eliminate the residual nitrates
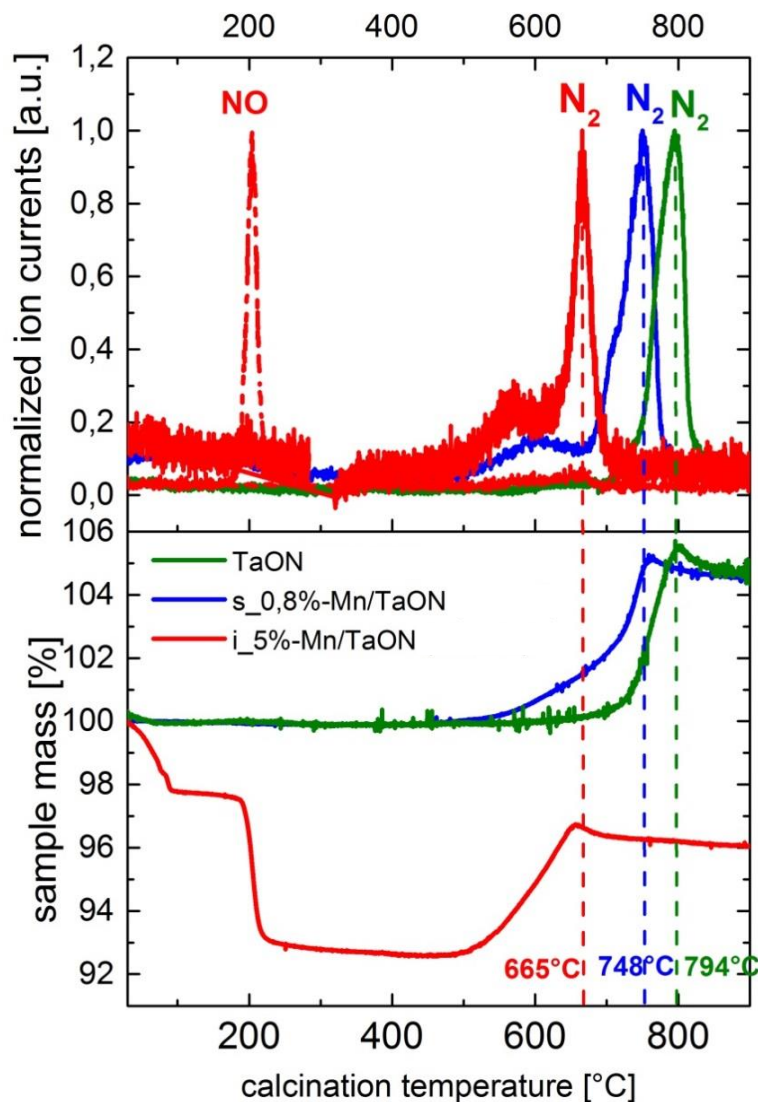


Figure 27: TGMS curves of different loaded TaON

## b) XRD of the loaded sample

MnOx is never to be seen in the XRD diffractogram of the loaded TaON because of its low loading, low particle size and/or amorphous character. It was noticed that the unstrained TaON structure remained unaffected up to calcination conditions of 400°C,10h. In contrast to this, Mn-loaded samples calcined at 400°C, 10h, showed clear straining of the TaON structure, whatever synthesis method was used cf Figure 28.
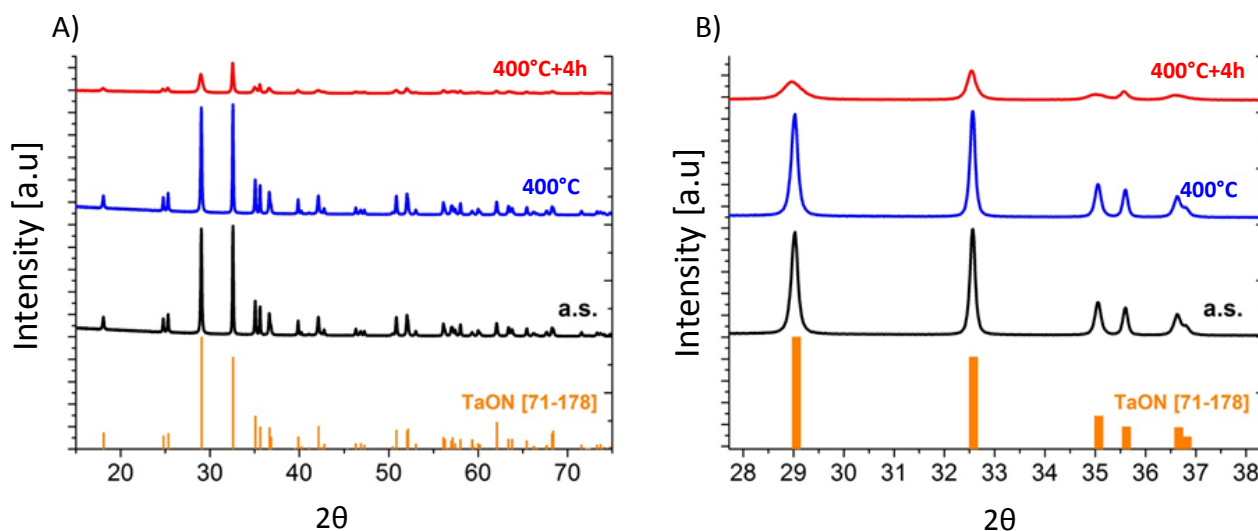


Figure 28: A) XRD diffractogram of 0,8%Mn loaded TaON at different moments of the calcination B) zoom on the 2θ=[28-38] region

In order to understand this phenomenon and possibly link it to the TGMS observations, in-situ XRD was performed on Mn-loaded samples in artificial air and Ar-atmosphere. This showed that in Ar, Mn-loaded samples don't strain, whereas in artificial air, after 4h at 400°C, there is a clear straining.

|  | Calcination atmosphere | 400°C | 400°C+4h |
|---|---|---|---|
| TaON | Air | No modification | No modification |
| Mn-TaON | Air | No modification | Anisotrope peak broadening |
| Mn-TaON | Argon | No modification | No modification |

Table 2: Summary Table of the calcination observations at different temperatures and atmospheres

This confirms the idea that MnOx on the surface acts as a catalyst for activated oxygen species that oxidizes the TaON surface. After several hours, straining is induced by the formation of surface $Ta_2O_5$. These results show a high sensitivity of TaON to the oxygen partial pressure, temperature and transition metal impurities that might explain the different variants of this material (yellow, green and strained, unstrained) from different synthesis batches. TEM of the Mn-loaded 400°C, 10h-calcined samples should confirm the presence of similar stacking faults than in the pure strained TU-samples and traces of $Ta_2O_5$ on the surface.

As a consequence, calcination temperature appears as a critical parameter as it is used to activate the Mn co-catcalyst but must be chosen in order to avoid the Mn-activated oxidative decomposition of the photocatalyst. We decided to stay below 400°C.

*c) Influence of the loading procedure: impregnated samples*

In order to study the influence of synthesis conditions on the electrochemical OER activity of the co-catalyst, we used the CAN-test. This test can't give us information about photocatalytic activity, but allows us to better understand the influence of synthesis parameters on the activity of the Mn-co-catalyst. Figure 29 represents the oxygen production per gram of manganese over time.
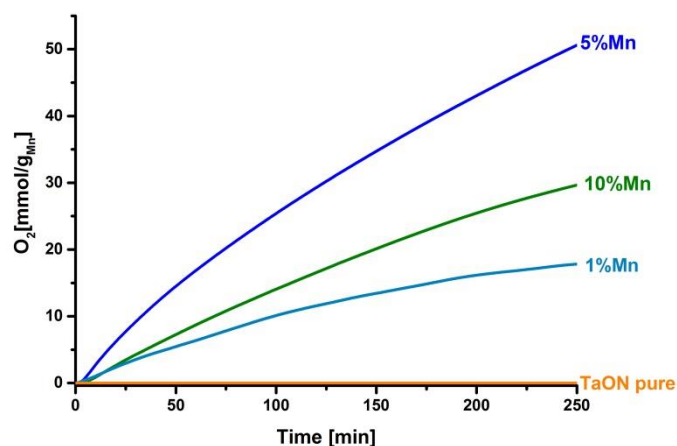


Figure 29: Oxygen production of the different manganese loaded samples over time

Photocatalytic activity is excluded as the test is performed under dark conditions. The activity observed for the loaded samples only corresponds to the OER-activity of the loaded manganese, which is, as seen before, a well-known water oxidation catalyst. The oxygen evolution curves show an increase of activity between 1% and 5%. It seems that the more manganese there is in the system, the better the activity. But the 10% loaded sample shows a lower activity than the 5% one, leading us to think that there is a saturation phenomenon.
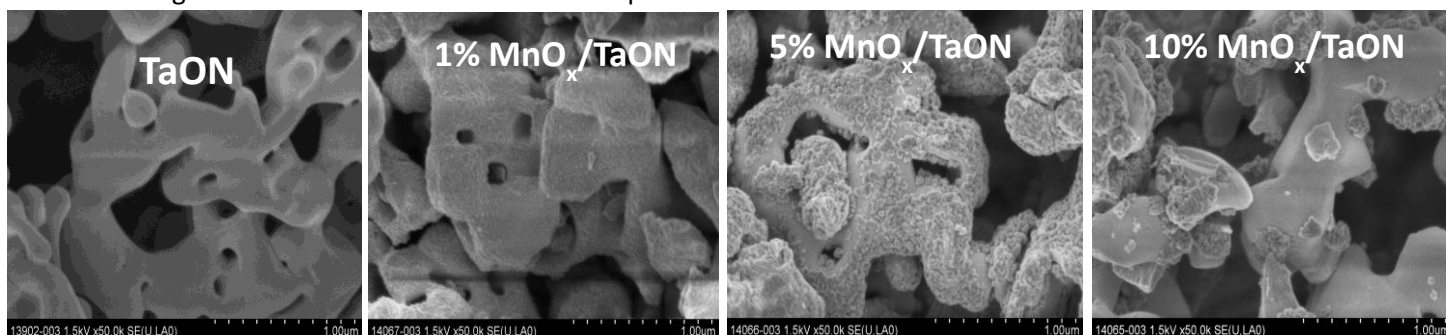


Figure 30: SEM pictures of TaON with different manganese loadings

This theory was subsequently validated with the SEM investigation presented figure 30. As we can see, the 1% loaded sample shows a very homogenous dispersion of the slightly rough Mn species at the surface of the TaON. The 5%loaded sample shows a thicker surface layer of the manganese and the presence of few aggregates. Finally, the 10%loaded sample shows a very poor dispersion and the presence of large aggregates with clean TaON surface between them. The loss of activity of the 10%loaded sample, despite its high manganese loading, can be explain by the formation of these large clusters, that reduces the specific surface of the active material.

## d) Influence of the loading procedure: deposition-precipitation

The impregnated samples were compared to the symproportionated samples in order to assess the influence of the synthesis pathway on the co-catalyst's OER-activity.
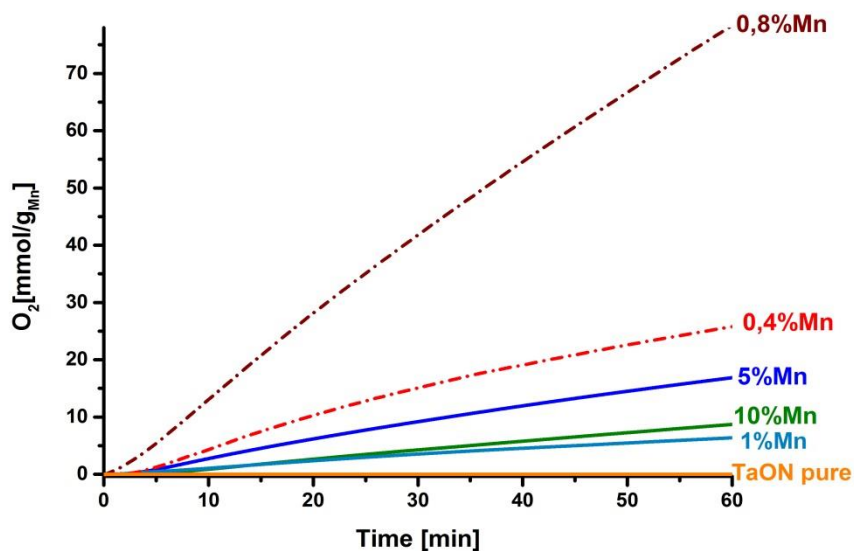


Figure 31: Oxygen production of the different manganese loaded samples over time. Dash lines: symproportionated samples. Full lines: impregnated samples

As we can see on figure 31, the symproportionated samples, even with very low co-catalyst amount show a very high activity per gramm of manganese. After one hour of reaction, the 0,8%symproportionated sample shows an activity more than 10times bigger than the one of the 1%impregnated sample.
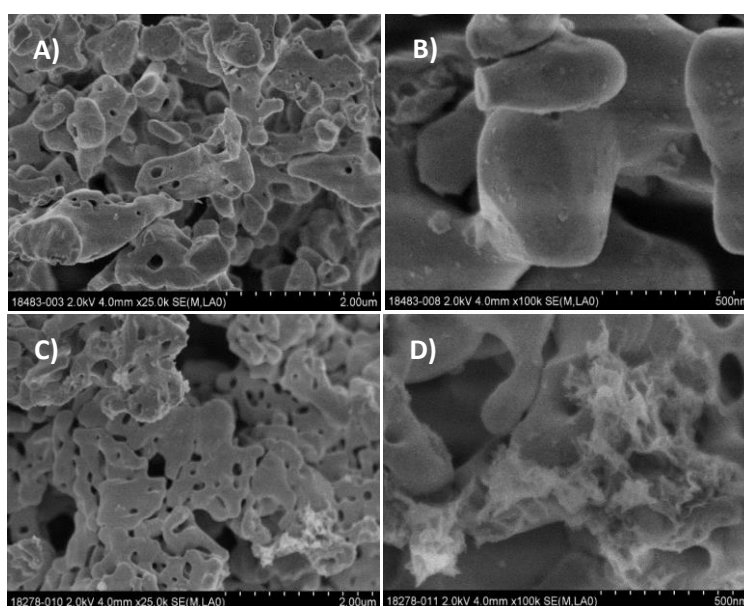


Figure 32: SEM pictures of A) 0,4%Mn-loaded TaON – impregnation B) Enlargment of picture A. C) 0,4%Mn-loaded TaON – deposition-precipitation D) Enlargment of picture C.

These differences in the activity of manganese for the two preparation methods, can come, on the one hand from morphological differences or, on the other hand, from the nature of the synthesized manganese oxides. As the preparation paths are very different, we expect to obtain different crystalline phases, or different oxidation states of the manganese oxides.

The SEM investigations presented figure 32, show that there are indeed, for two equally loaded samples, morphological differences between the two preparation methods. The deposition-precipitation method leads to the formation of large non-homogenous aggregates at the surface of the TaON (figure 32)C) and D)) while the impregnation method leads to the formation of very small and nearly one dimensional particles (figure 32)B) and C)). Furthermore the impregnation method seems to have partially destroyed the TaON (factures of the material can be observed figure 32)B). These differences in the activity of the samples is attributed to the fact that sympropotionation yields active Mn(IV) species, while the impregnated sample are based on Mn(II) before thermal treatment

### f) Influence of the pH control agent
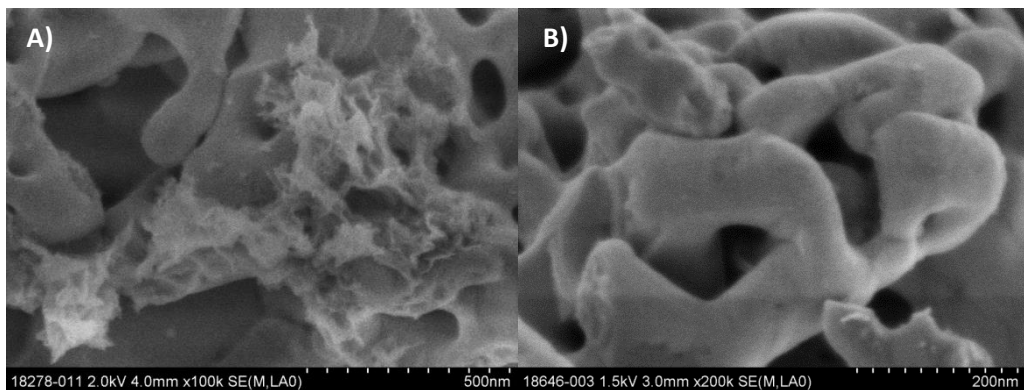


Figure 33: SEM pictures of A) 0,4%Mn-loaded TaON symproportionation using NaOH B) 0,4%Mn-loaded TaON symproportionation using NH$_4$OH

SEM was used to study the influence of the pH-control agent on the morphology of the samples. The two alkaline solutions that were used for this study were NaOH and NH$_4$OH. As we can see figure 33)A) the use of NaOH leads to the formation of large agglomerates at the surface of the TaON, whereas the use of NH$_4$OH leads to a very smooth surface Figure 33)B). This very smooth surface can be explained by: the absence of manganese, or a very homogeneous repartition of very small particles. XRF analysis was performed in order to determine the presence or absence of manganese, and revealed that 0,30% in mass of the sample corresponds to manganese, in reasonable agreement with the nominal value. In order to verify that this amount corresponds to manganese particles adsorbed at the surface of the TaON, and not to a free solid, TEM investigations were conducted.

1. *TEM investigations of the Symproportionated sample using NH₄OH*
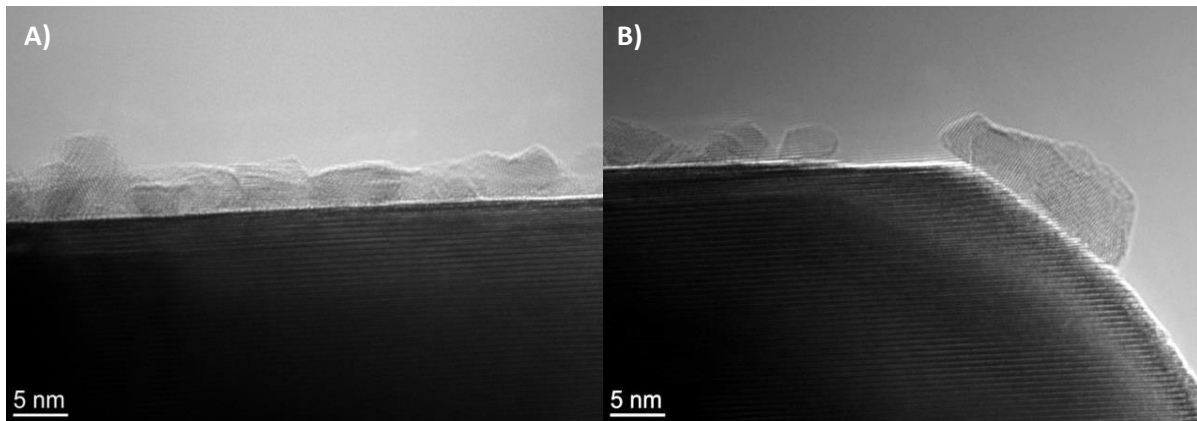


Figure 34: TEM pictures of the TaON surface. Sample symproportionated with NH$_4$OH [0,4%Mn]

The dark material in figure 34)A and B) was identified as TaON and the small particles on the surface as manganese thanks to EDX analysis. Figure 34)A) validates the theory of a very thin and homogeneous manganese layer at the surface of the TaON. Figure 34)B) shows us that despite the high dispersion of the manganese, we can observe some isolated, but still relatively small particles.

2. *TEM investigations of the symproportionated sample using NaOH*
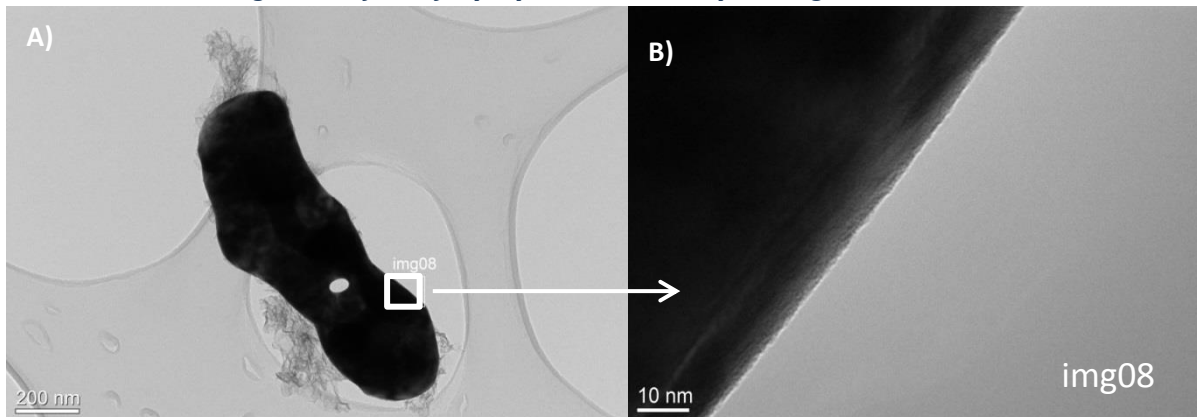


Figure 35: TEM pictures of the TaON surface. Sample symproportionated with NaOH [0,4%Mn]

In order to confirm the fact that this homogeneous manganese layer war only to be found on samples using NH$_4$OH as a pH-control agent, TEM investigations were also led on the sample synthesized with NaOH.

The dark material in Fig 35)A) and B) was identified as TaON and the big clusters on the surface as manganese thanks to EDX analysis. As presented on the SEM picture Figure 32)D), we can observe with TEM the same unorganized clusters at the surface of the TaON. Between those clusters, no manganese layer was to be seen.

These differences can be explained by the fact that NH$_4$OH is a very good ligand for transition metal cations. In presence of a complexating agent, Mn$^{2+}$ ions won't tend to agglomerates.

Furthermore, the use of a non-metallic alkaline solution, avoid the inclusion of impurities in the sample. [Na could sit in the interstitial site of the manganese oxides and thereby contaminate the material].

# Conclusion and outlook

During this project, we studied TaON as a photocatalytic material, and the possibility of enhancing its activity by loading it with a Mn-based co-catalyst.

Some TaON samples presented anomalies: straining or colour changes. These anomalies were attributed to lattice imperfections and oxygen vacancies. They were shown to have a negative influence on the photocatalytic activity of the material. This deterioration was attributed to the presence of structural defects, acting as recombination centres for photogenerated charge carriers. The resulting increase in recombination kinetics lowers the photocatalytic activity of these samples.

The same straining effect appeared during calcination of the Mn-loaded samples. After four hours at 400°C in synthetic air, we observe a large anisotropic peak broadening in the XRD patterns of the samples. This phenomenon couldn't be observed when calcining in Ar. TGMS and XRD analysis tend to confirm the hypothesis that MnOx on the surface acts as a catalyst for activated oxygen species, which oxidizes the TaON surface. This phenomenon has to be avoided by any means as it leads to the creation of an inactive, passivating $Ta_2O_5$ layer.

The loading procedure was shown to have a great influence on the distribution, dispersion and morphology of loaded co-catalyst and on its electrochemical OER activity. Even at low loadings, samples obtained by constant-pH symproportionation showed an electrocatalytic activity ten times higher as compared to the impregnated samples. Excessive loading might lead to a lower electrocatalytic activity by decreasing the specific surface, however it is also clear from the results that the MnOx phase formed by symproportionation is much more active for OER, probably due to a higher concentration of active OER-sites. This is attributed to the fact that sympropotionation yields active Mn(IV) species, while the impregnated sample are based on Mn(II) before thermal treatment.

Having showed more promising results, we deepened our investigations on the deposition-precipitation procedure, and studied the influence of the pH-control agent on the morphology of the samples. NaOH showed the formation of large manganese clusters while the use of $NH_4OH$ led to small particles homogeneously dispersed at the surface of the TaON. This is likely a result of the complexating effect of the $NH_3$ ligands, which helps to avoid aggregation of Mn-species.

Photocatalytic tests are currently under way on the Mn-loaded TaON in order to determine the optimal Mn-loading required to enhance the overall photocatalytic OER activity of the samples. Not only has the co-catalyst to be active, but the absorption of light by the TaON must remain unhindered. If an optimal Mn-loading ratio can be determined by these means, this would constitute a promising advance in the quest for a visible-light absorbing OER photocatalyst enhanced by earth-abundant Mn-co-catalysts.

# Bibliography

(1)     Peilin Liao, J. A. K. *Journal of the American Chemical Society* **2012**, *134*, 13296.
(2)     Chen, Y.; Cui, P.; Xiong, G.; Xu, H. *Asia-Pacific Jrnl of Chem. Eng* **2010**, *5*, 93.
(3)     Chen, X.; Shen, S.; Guo, L.; Mao, S. S. *Chem. Rev.* **2010**, *110*, 6503.
(4)     Liao, C.-H.; Huang, C.-W.; Wu, J. C. S. *Catalysts* **2012**, *2*, 490.
(5)     Fujishima, A.; Honda, K. *Nature* **1972**, *238*, 37.
(6)     Maeda, K.; Domen, K. *J. Phys. Chem. C* **2007**, *111*, 7851.
(7)     Osterloh, F. E. *Chem. Soc. Rev.* **2013**, *42*, 2294.
(8)     Maeda, K. *Journal of Photochemistry and Photobiology C-photochemistry Reviews - J PHOTOCHEM PHOTOBIOL C-PHOTO* **2011**.
(9)     Sayama, K.; Arakawa, H. *J. Chem. Soc., Faraday Trans.* **1997**, *93*, 1647.
(10)    Hisatomi, T.; Hasegawa, K.; Teramura, K.; Takata, T.; Hara, M.; Domen, K. *Chemistry Letters* **2007**, *36*, 558.
(11)    Xiao, W.; Yuan, J.; Zhang, Y.; Shangguan, W. *Materials Chemistry and Physics* **2007**, *105*, 6.
(12)    Bao, N.; Shen, L.; Takata, T.; Domen, K. *Chem. Mater.* **2008**, *20*, 110.
(13)    Yan, H.; Yang, J.; Ma, G.; Wu, G.; Zong, X.; Lei, Z.; Shi, J.; Li, C. *Journal of Catalysis* **2009**, *266*, 165.
(14)    Maeda, K.; Teramura, K.; Saito, N.; Inoue, Y.; Domen, K. *Journal of Catalysis* **2006**, *243*, 303.
(15)    Cook, T. R.; Dogutan, D. K.; Reece, S. Y.; Surendranath, Y.; Teets, T. S.; Nocera, D. G. *Chem. Rev.* **2010**, *110*, 6474.
(16)    Abe, T.; Suzuki, E.; Nagoshi, K.; Miyashita, K.; Kaneko, M. *J. Phys. Chem. B* **1999**, *103*, 1119.
(17)    Youngblood, W. J.; Lee, S.-H. A.; Maeda, K.; Mallouk, T. E. *Acc. Chem. Res.* **2009**, *42*, 1966.
(18)    Singh, A.; Chang, S. L. Y.; Hocking, R. K.; Bach, U.; Spiccia, L. *Energy Environ. Sci.* **2013**, *6*, 579.
(19)    Maeda, K.; Lu, D.; Domen, K. *Chem. Eur. J.* **2013**, *19*, 4986.
(20)    Higashi, M.; Domen, K.; Abe, R. *Journal of the American Chemical Society* **2012**, *134*, 6968.
(21)    Armytage, D.; Fender, B. E. F. *Acta Crystallographica Section B Structural Crystallography and Crystal Chemistry* **1974**, *30*, 809.
(22)    Strähle, J. *Z. anorg. allg. Chem.* **1973**, *402*, 47.
(23)    Hitoki, G.; Takata, T.; Kondo, J. N.; Hara, M.; Kobayashi, H.; Domen, K. *Chem. Commun.* **2002**, 1698.
(24)    Lubitz, W.; Reijerse, E. J.; Messinger, J. *Energy Environ. Sci.* **2008**, *1*, 15.
(25)    Nocera, D. G. *Acc. Chem. Res.* **2012**, *45*, 767.
(26)    Wiechen, M.; Zaharieva, I.; Dau, H.; Kurz, P. *Chem. Sci.* **2012**, *3*, 2330.
(27)    Umena, Y.; Kawakami, K.; Shen, J.-R.; Kamiya, N. *Nature* **2011**, *473*, 55.
(28)    Man, I. C.; Su, H.-Y.; Calle-Vallejo, F.; Hansen, H. A.; Martínez, J. I.; Inoglu, N. G.; Kitchin, J.; Jaramillo, T. F.; Nørskov, J. K.; Rossmeisl, J. *ChemCatChem* **2011**, *3*, 1159.
(29)    Wiechen, M.; Berends, H.-M.; Kurz, P. *Dalton Trans* **2012**, *41*, 21.
(30)    Boppana, V. B. R.; Jiao, F. *Chem. Commun.* **2011**, *47*, 8973.
(31)    Mette, K.; Bergmann, A.; Tessonnier, J.-P.; Hävecker, M.; Yao, L.; Ressler, T.; Schlögl, R.; Strasser, P.; Behrens, M. *ChemCatChem* **2012**, *4*, 851.
(32)    Ahmed, K. A. M.; Peng, H.; Wu, K.; Huang, K. *Chemical Engineering Journal* **2011**, *172*, 531.
(33)    Jiao, F.; Frei, H. *Energy Environ. Sci.* **2010**, *3*, 1018.
(34)    Iyer, A.; Del-Pilar, J.; King'ondu, C. K.; Kissel, E.; Garces, H. F.; Huang, H.; El-Sawy, A. M.; Dutta, P. K.; Suib, S. L. *J. Phys. Chem. C* **2012**, *116*, 6474.
(35)    Gorlin, Y.; Jaramillo, T. F. *Journal of the American Chemical Society* **2010**, *132*, 13612.
(36)    Nakagawa, T.; Bjorge, N. S.; Murray, R. W. *Journal of the American Chemical Society* **2009**, *131*, 15578.
(37)    Surendranath, Y.; Dincă, M.; Nocera, D. G. *Journal of the American Chemical Society* **2009**, *131*, 2615.
(38)    Parent, A. R.; Crabtree, R. H.; Brudvig, G. W. *Chem. Soc. Rev.* **2013**, *42*, 2247.

(39)     Hayes, S. A.; Yu, P.; O'Keefe, T. J.; O'Keefe, M. J.; Stoffer, J. O. *J. Electrochem. Soc.* **2002**, *149*, C623.

(40)     Takata, T.; Hitoki, G.; Kondo, J. N.; Hara, M.; Kobayashi, H.; Domen, K. *Res. Chem. Intermed.* **2007**, *33*, 13.

(41)     Hara, M.; Hitoki, G.; Takata, T.; Kondo, J. N.; Kobayashi, H.; Domen, K. *Catalysis Today* **2003**, *78*, 555.

(42)     Wang, X.; Maeda, K.; Thomas, A.; Takanabe, K.; Xin, G.; Carlsson, J. M.; Domen, K.; Antonietti, M. *Nat Mater* **2009**, *8*, 76.

(43)     Bredow, T.; Lumey, M.-W.; Dronskowski, R.; Schilling, H.; Pickardt, J.; Lerch, M. *Z. anorg. allg. Chem.* **2006**, *632*, 1157.

(44)     Sun, Y.; Thompson, S. E.; Nishida, T. *Journal of Applied Physics* **2007**, *101*.

(45)     Chun, W.-J.; Ishikawa, A.; Fujisawa, H.; Takata, T.; Kondo, J. N.; Hara, M.; Kawai, M.; Matsumoto, Y.; Domen, K. *J. Phys. Chem. B* **2003**, *107*, 1798.

(46)     Zetasizer Nanoseries MALVERN instrument- User Manual

# Webography

(a)   http://www.chevron.com/globalissues/energysupplydemand/

(b)   http://www.energie-environnement.ch

(c)   http://www.nrel.gov/

(d)   http://www.semos.dk/Per/41653/download/Pourbaix_multielement_systems.pdf

# APPENDIX

## 1) Zeta Potential measurements[46]

### a) Theory

When a charged particle is suspended in a liquid, particles of the opposite charge will be attracted to its surface. Ions close to the surface of the charged particle are strongly bound to it and form the "stern layer", whereas ions that are further away are loosely bound and form the "diffuse layer". Within the diffuse layer there is an immaterial boundary; any ion within this boundary will move with the particle when it's moving in the liquid, and any particle outside of it won't. This boundary is called the slipping plane (cf. Figure 36-A). The electrical potential that exists at this boundary is known as the zeta potential. The most important factor that affects zeta potential is the pH.

To each pH corresponds a zeta potential value. Indeed if a particle is charged negatively in a neutral solution, and that we add base to the suspension, the particle will tend to acquire a more negative charge. On the other hand, if we add progressively an acid, the negative charge will be progressively neutralized, and then build up a positive charge. Therefore, there is a specific pH at which the zeta potential equals zero: the isoelectric point (cf. Figure 36-B).
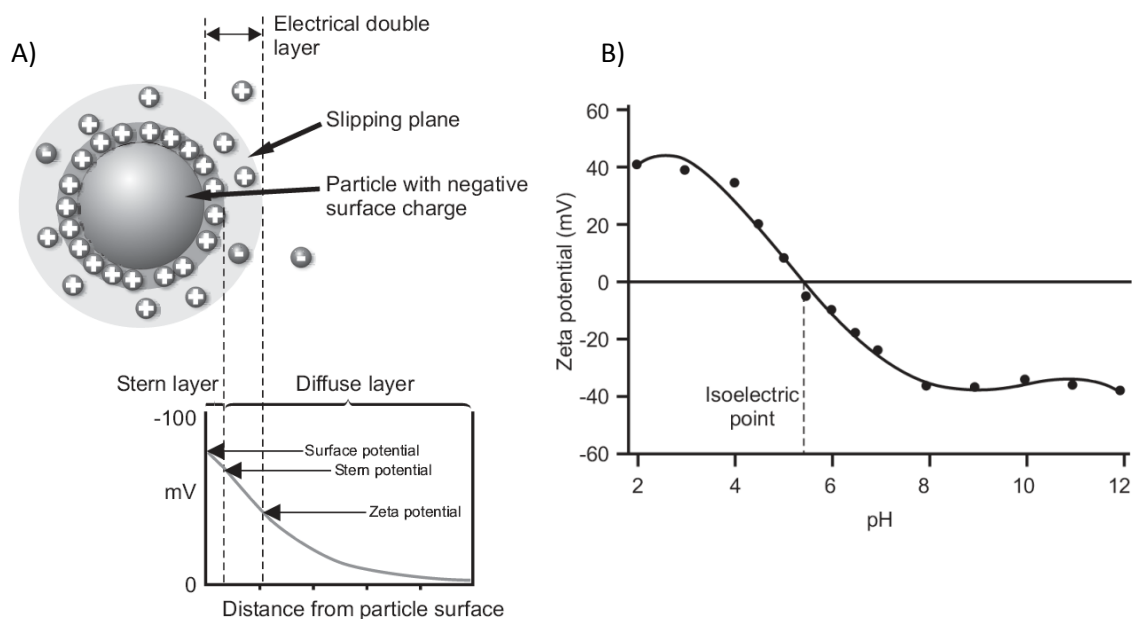


Figure 36: A) Representation of the different layers at the surface of a particle in solution. B) General evolution of the Zeta Potential as a function of the pH

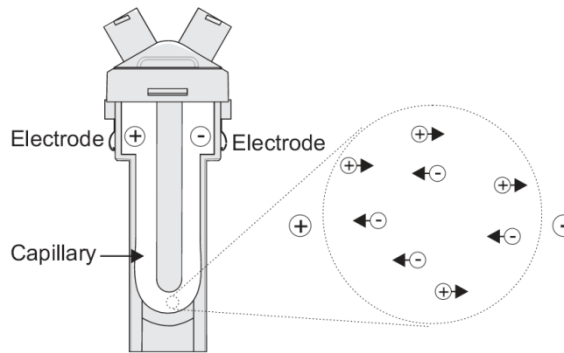*b) How does the instrument measures zeta potential*



Figure 37: Measurement cup used inside of the Zeta Sizer

When an electric field is applied across a suspension, charged particles are attracted towards the electrode of the opposite charge (cf. Figure 37). Viscosity tends to slow down this movement. When equilibrium is reached between these two opposing forces, the particles move with a constant velocity. The velocity of the particle depends on the following factors: strength of the electric field applied, dielectric constant of the solution, viscosity of the solution, and the zeta potential.

Velocity is defined by the Henry equation: $$U = \frac{2\varepsilon z\, f(Ka)}{3\eta}$$

Z: Zeta Potential           ε: dielectric constant
U: Velocity                 η: Viscosity
f(Ka): Henry's function (=1,5 for aqueous solution)
The measuring device uses "Laser Doppler Velocimetry"(LVD) to determine the particles velocity, from which we get the Zeta potential.

## 2) XRD measurements

The X-ray crystallography is an analysis method used to determine the atomic and molecular organization of a crystal. It is based on the interaction of X-ray radiations with a crystalline (or semi-crystalline) material (no liquids, no amorphous polymer, no glass..). When the incident X-ray beam meets the crystalline sample, it is diffused in many directions; this diffusion can be incoherent (Compton's diffusion) or coherent (Rayleigh's diffusion) also called diffraction. The diffraction phenomenon is described by Bragg's law:  $2d_{hkl}\sin\theta = n\lambda$  (Figure 18)
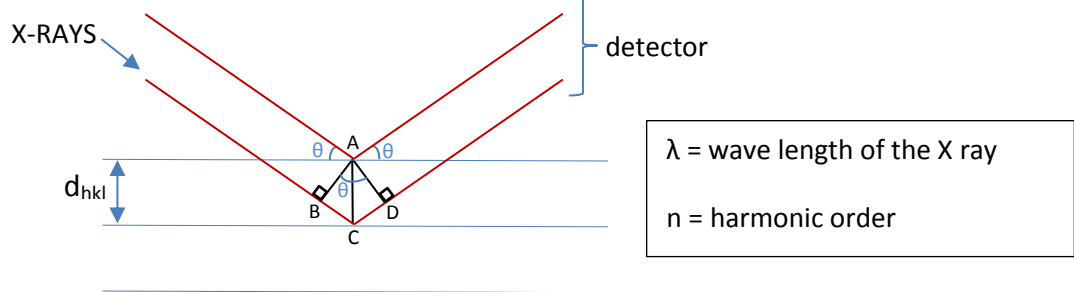


λ = wave length of the X ray

n = harmonic order

Figure 38: X-RAYS incidence in the material

Diffraction conditions :    BC+CD=2   ;    BC=$d_{hkl}\sin\theta$   ;   BC=nλ  ;   n= natural number

The two dimensional pattern obtained by the detector under different angles are converted into a three dimensional model of the electronic density of the crystal using Fourier transforms. Out of this method we can determine the atomic structure of the sample.

### 3) TGMS measurements

During a standard thermogravimetric analysis (TGA), the variations of the mass of a sample are monitored while it's been progressively heated to high temperatures. A variation of the mass of a sample can be observed when, for example, adsorbed species are evaporated or when it decomposes. Every loss of mass corresponds to a particular reaction from which the gaseous product is detected by a mass spectrometer. This method makes the interpretation of thermogravimetric analysis much easier and more reliable.

This analysis, allow us to determine important synthesis parameters such as the drying and calcination times and temperatures.

Furthermore, thanks to the differential scanning calorimetry (DSC), we can know if the reactions observed, are consuming or releasing energy, that is to say if they are endo- or exothermic.

### 4) SEM EDX analysis

SEM-EDX stands for scanning electron microscopy with energy dispersive X-ray spectroscopy. With the scanning electron microscopy we can obtain high resolution images of a surface topography; for this a scanning electron beam is directed to the sample. This electron beam will be referred as "primary". The primary electrons hit the surface of the sample with an energy of 0,5 to 30kV and this will generates secondary electrons. The intensities of the secondary electrons depends on the surface topography, and thanks to this secondary beam we will be able to reconstruct a map of the sample's surface.

In addition to secondary electrons, the primary electron bombardment is also going to induce X-rays. The intensity of the produced X-rays is correlated to the atomic number of the elements bombarded. And as the primary beam can be extremely precise, it makes it possible to analysis the elemental composition of definite spots of the sample's surface.

SEM-EDX is considered a relatively rapid and non-destructive qualitative and semi-quantitative approach to surface analysis.

### 5) TEM analysis

The transmission electron microscopy (TEM) is based on the same principle as a classic light microscope, but instead of a light beam going through the sample, it is bombarded with an electron beam. For this aim the samples need to be extremely thin.

The electron beam will, as it passes through the sample, interact with it, and it is from these interactions that an image will be obtained. The contrasts observed in the produced image, correspond to the partial absorption of electrons in the material: it can be due to the thickness of the sample or, more interestingly, to its composition.

## 6) TPRL measurements

The TRPL (Time-Resolved Photoluminescence) is a method that allows us to determine the life-time of charge carriers in semiconductor materials. Photoluminescence describes the emission of light by a material after photoexcitation. The period between excitation and emission is called the life time of charge carriers. TPRL is measured by exiting a sample with photons and then measuring the decay in photoluminescence as a function of time.

## 7) XRF analysis

XRF (for X-ray fluorescence) is an elemental analysis based on the emission of secondary X-rays. For the measure, a sample is strike with x-rays. Those x-rays have a sufficient energy to eject electrons from the inner shell, creating vacancies. These vacancies make the atom instable, and electrons from the outer shell are transferred to the inner shell to come back to a stable state. This process gives off a characteristic x-ray. The energy of this secondary x-rays depends on the energy level of the atom, and is, for this reason, characteristic of the element bombarded.

## 8) Strain factor calculus

The XRD patterns were analyzed by whole pattern fitting using the TOPAS software [TOPAS version 4.2, (c) 1999, 2009 Bruker AXS, Karlsruhe]. The sample related broadening of the diffraction peaks is caused by imperfections of the crystal lattice, like finite crystallite size and microstrain (local distortions of lattice planes).

In the case of isotropic peak broadening, which is independent from the direction in the crystallites and thus from *hkl*, the contributions of size and strain broadening can be separated due to their different dependence from the Bragg angle θ (size broadening is proportional to 1/cos(θ), while strain broadening is proportional to tan (θ)).

However, most of the TaON samples exhibit a more or less pronounced anisotropic peak broadening, which means that the peak width is predominantly a function of *hkl* rather than θ, because at least one of the broadening components is dependent from the direction in the crystal. In this case, there is no theoretical basis available for a reliable deconvolution of size and strain broadening. Thus, a simplified model was developed to extract at least tentative size and strain values. Instead of whole pattern fitting, this model analyzes only the broadening of the two most prominent peaks, 1 −1 −1 and 1 1 1. In samples with obvious anisotropy, the 1 −1 −1 reflection is among the most broadened, while 1 1 1 is among the sharpest. Thus, we make the following simplifying assumptions:

(a) In the 1 1 1 direction, the strain is negligible, i.e. the broadening is attributed to size only. This means that the estimated crystallite size is extracted directly from the 1 1 1 broadening.

(b) The anisotropy is caused by strain only, while the size broadening is isotropic. Thus, the same size value obtained from the 1 1 1 reflection is also applied to the 1 −1 −1 peak, allowing the calculation of strain in this direction from the remaining peak broadening.

(c) Even though the observed strain is anisotropic, we assume that the strain obtained for the 1 −1 −1 direction is a representative measure for the property of strain in general, and thus scales with the amount of defects which cause it.